Constraints on the shallow velocity structure of the Lucky Strike Volcano, Mid-Atlantic Ridge, from downward continued multichannel streamer data

A. F. Arnulf, A. J. Harding, G. M. Kent, S. C. Singh, W. C. Crawford

▶ **To cite this version:**

A. F. Arnulf, A. J. Harding, G. M. Kent, S. C. Singh, W. C. Crawford. Constraints on the shallow velocity structure of the Lucky Strike Volcano, Mid-Atlantic Ridge, from downward continued multichannel streamer data. Journal of Geophysical Research : Solid Earth, 2014, 119, pp.1119-1144. 10.1002/2013JB010500 . insu-03581147

HAL Id: insu-03581147

https://insu.hal.science/insu-03581147

Submitted on 19 Feb 2022

HAL is a multi-disciplinary open access archive for the deposit and dissemination of scientific research documents, whether they are published or not. The documents may come from teaching and research institutions in France or abroad, or from public or private research centers.

L'archive ouverte pluridisciplinaire **HAL**, est destinée au dépôt et à la diffusion de documents scientifiques de niveau recherche, publiés ou non, émanant des établissements d'enseignement et de recherche français ou étrangers, des laboratoires publics ou privés.

Copyright

AGU PUBLICATIONS

JGR

Journal of Geophysical Research: Solid Earth

RESEARCH ARTICLE
10.1002/2013JB010500

Key Points:
- A new method to create high-resolution tomographic images of the oceanic crust.
- The central part of the Lucky Strike segment is shown to be anomalously magmatic
- Hydrothermal sealing of porosity is progressing at normal to enhanced rates

Supporting Information:
- Readme
- Figure S1

Correspondence to:
A. F. Arnulf,
aarnulf@ucsd.edu

Citation:
Arnulf, A. F., A. J. Harding, G. M. Kent, S. C. Singh, and W. C. Crawford (2014), Constraints on the shallow velocity structure of the Lucky Strike Volcano, Mid-Atlantic Ridge, from downward continued multichannel streamer data, *J. Geophys. Res. Solid Earth*, *119*, 1119–1144, doi:10.1002/2013JB010500.

Received 8 JUL 2013
Accepted 8 JAN 2014
Accepted article online 14 JAN 2014
Published online 13 FEB 2014

Constraints on the shallow velocity structure of the Lucky Strike Volcano, Mid-Atlantic Ridge, from downward continued multichannel streamer data

A. F. Arnulf[1], A. J. Harding[1], G. M. Kent[2], S. C. Singh[3], and W. C. Crawford[3]

[1]Cecil H. and Ida M. Green Institute of Geophysics and Planetary Physics, Scripps Institution of Oceanography, University of California San Diego, La Jolla, California, USA, [2]Nevada Seismological Laboratory/0174, University of Nevada, Reno, Reno, Nevada, USA, [3]Laboratoire de Géosciences Marines, Institut de Physique du Globe de Paris, Paris, France

Abstract The shallow velocity structure of the Lucky Strike segment of the Mid-Atlantic Ridge is investigated using seismic refraction and reflection techniques applied to downward continued multichannel streamer data. We present a three-dimensional velocity model beneath the Lucky Strike Volcano with unprecedented spatial resolutions of a few hundred meters. These new constraints reveal large lateral variations in *P* wave velocity structure beneath this feature. Throughout the study area, uppermost crustal velocities are significantly lower than those inferred from lower resolution ocean bottom seismometer studies, with the lowest values (1.8–2.2 km/s) found beneath the three central volcanic cones. Within the central volcano, distinct shallow units are mapped that likely represent a systematic process such as burial of older altered surfaces. We infer that the entire upper part of the central volcano is young relative to the underlying median valley floor and that there has been little increase in the layer 2A velocities since emplacement. Layer 2A thins significantly across the axial valley bounding faults likely as the result of footwall uplift. The upper crustal velocities increase with age, on average, at a rate of ~0.875 km/s/Myr, similar to previous measurements at fast-spreading ridges, suggesting hydrothermal sealing of small-scale porosity is progressing at normal to enhanced rates.

1. Introduction

Since the early seismic investigations of mid-ocean ridge crest structure in the mid-1970s [e.g., *Orcutt et al.*, 1976], numerous active-source seismic surveys have been conducted to study the emplacement, structure, and evolution of the oceanic crust. These experiments have provided evidence for a relatively uniform crustal structure at fast-spreading ridges, but a much more heterogeneous structure at their slow-spreading counterparts, indicative of a more complex origin and evolution.

With the exception of some specific features like transform faults, propagating rifts, and overlapping spreading centers (OSCs) [see: *Macdonald and Fox*, 1983; *Carbotte and Macdonald*, 1992; *Kent et al.*, 2000; *Combier et al.*, 2008], fast-spreading ridges present a quasi two-dimensional structure, with a relatively simple morphology [*Macdonald*, 1982, 2001], a well-defined seismic structure [*Harding et al.*, 1989; *Vera et al.*, 1990; *Harding et al.*, 1993; *Kent et al.*, 1993] and a quasi steady state melt body [*Detrick et al.*, 1987; *Singh et al.*, 1998; *Carbotte et al.*, 2000].

Slow-spreading ridges, on the other hand, show greater three-dimensional structure, with a much rougher surface morphology [*Macdonald*, 1982; *Tucholke and Lin*, 1994] and heterogeneous seismic structure [*Tolstoy et al.*, 1993; *Hooft et al.*, 2000; *Arnulf et al.*, 2011, 2012]. While melt bodies have been imaged beneath some segment centers [*Sinha et al.*, 1998; *Singh et al.*, 2006], others show no melt body [*Detrick et al.*, 1990] and in no instance has a continuous melt body been observed beneath an entire segment. Seafloor outcrops also exhibit great diversity, with pillow lavas, dikes, gabbros, and even ultramafics found in seafloor samples [*Cannat et al.*, 1995; *Blackman et al.*, 2002; *Boschi et al.*, 2006]. Strong tectonic processes are evidenced by detachment faults [*Cann et al.*, 1997; *Dick et al.*, 2008; *Canales et al.*, 2008; *Blackman and Collins*, 2010], axial valley faults and the preponderance of fractures and fissures.

In such a complicated environment, three-dimensional imaging is necessary to accurately characterize crustal structure and thus advance our understanding of crustal accretion. Three-dimensional active seismic refraction experiments using ocean bottom seismometers (OBSs) with deployments on a 5 km grid reveal crustal structure

©2014. American Geophysical Union. All Rights Reserved.

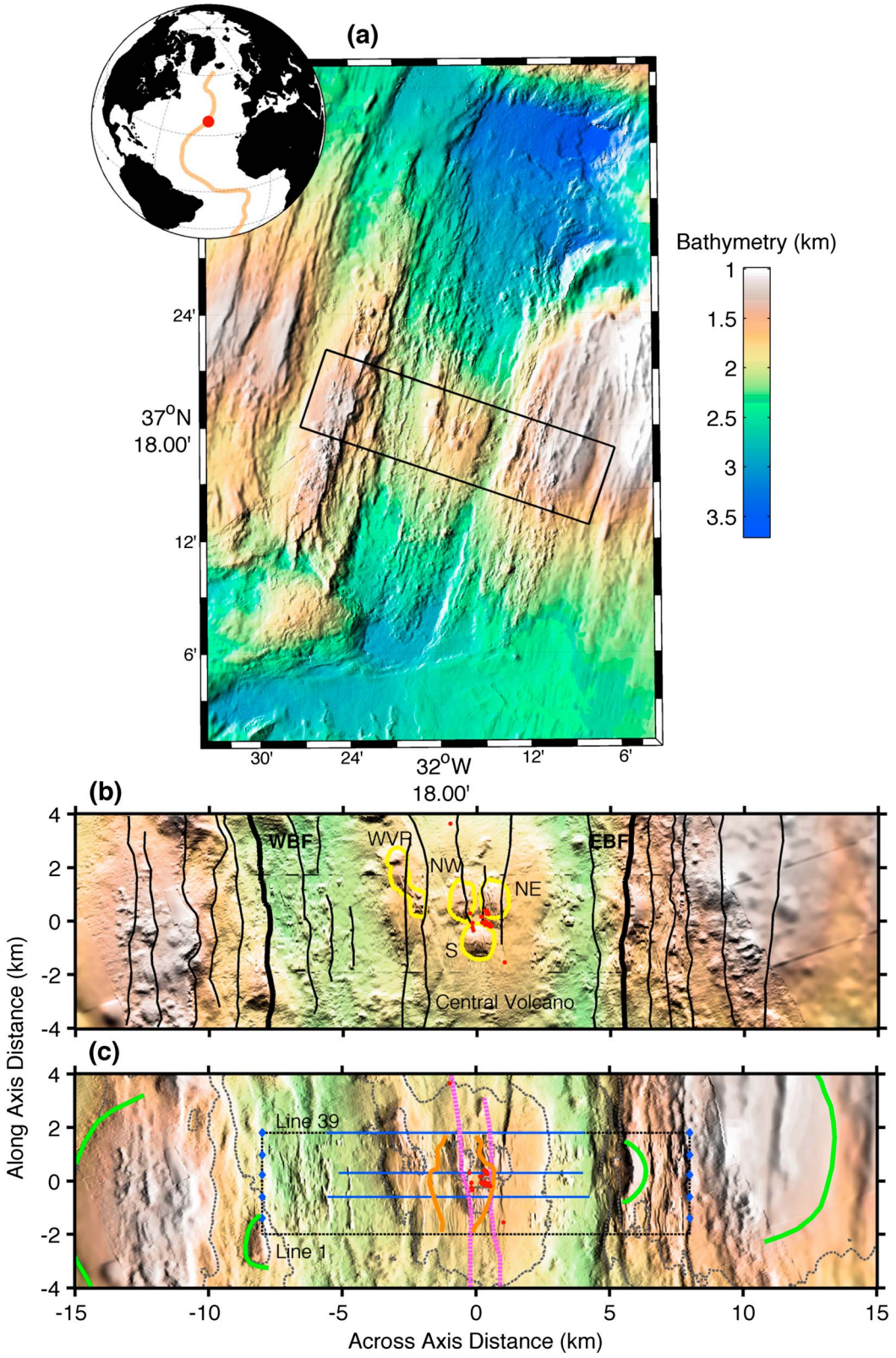

Figure 1

©2014. American Geophysical Union. All Rights Reserved.

at spatial scales approaching 5 km horizontally and 2 km vertically [*Seher et al*., 2010a], but do not typically have the spatial resolution needed for detailed studies of the uppermost crust [*Collins et al*., 2009].

In this paper, we use a combination of the Synthetic Ocean Bottom Experiment method (SOBE) [see *Harding et al*., 2007; *Arnulf et al*., 2011, 2012; *Henig et al*., 2012] and three-dimensional tomography to derive a high-resolution three-dimensional seismic tomographic image of the uppermost kilometer of oceanic crust at Lucky Strike Volcano on the Mid-Atlantic Ridge (MAR). The resulting velocity model reveals velocities within the uppermost crust (seismic layer 2A) with an unprecedented resolution of a few hundred meters, comparable to that of multichannel seismic (MCS) reflection imaging, and we use the final 3-D velocity structure to explore fundamental links between magmatic, tectonic, and hydrothermal processes beneath the Lucky Strike Volcano.

2. Background

The 70 km long Lucky Strike segment of the Mid-Atlantic Ridge (MAR) is centered at 37.3°N, south of the Azores triple junction. With a full spreading rate of 2.1 cm/yr [*Demets et al*., 1994], it is characterized by several features common to slow spreading segments, including a broad (15–20 km wide) median valley, nodal basins near the segment ends, and a topographic high at the segment center [*Fouquet et al*., 1995] (Figure 1).

The segment center is capped by the 0.3–0.4 km high, 7 km wide Lucky Strike Volcano, and the median valley is bounded by 0.5–0.9 km high escarpments known as the East and West Bounding Faults (EBF/WBF) [*Detrick et al*., 1995]. The Lucky Strike Volcano hosts three highly fractured summit volcanic cones made of highly vesicular volcanic breccias and pillows surrounding an unfaulted flat lava lake capped by fresh, low vesicularity massive lava flows [*Ondréas et al*., 1997, 2009; *Humphris et al*., 2002]. The lava lake is surrounded by an active hydrothermal field that consists of massive polymetallic sulfide deposits and standing inactive and active chimneys [*Ondréas et al*., 1997, 2009; *Humphris et al*., 2002] (Figure 1b). Vents within this field include high temperature, black smoker chimneys venting fluids up to 333°C [*Langmuir et al*., 1997]. A low magnetization anomaly coincident with the lava lake and surrounding hydrothermal field is likely the result of demagnetization of extrusive rocks by focused hydrothermal flow [*Miranda et al*., 2005]. A linear neovolcanic zone seen in side-scan sonar [*Scheirer et al*., 2000] and near-bottom observations [*Ondréas et al*., 2009], runs parallel to the rift valley walls and passes through the lava lake. Recent highly vesicular magmatism is also found on a volcanic edifice located northwest of the central volcano (the western volcanic ridge [*Fouquet et al*., 1994]). Finally, lobate lavas, draped lavas, and massive flows were recognized north of these three summit mounds in a ~2.5 km wide graben that lies between the lava lake and the western ridge and also parallels to the rift valley walls [*Ondréas et al*., 1997].

Rare gas analyses conducted by *Moreira and Allegre* [2002] suggest enhanced melt supply from the Azores hot spot, a proposition supported by the presence of anomalously shallow regions on both sides of the Lucky Strike segment, cut by V-shaped ridges propagating south from the Azores hot spot [*Cannat et al*., 1999; *Escartín et al*., 2001]. Teleseismic observations implying recent dike intrusion [*Dziak et al*., 2004], the discovery of an axial magma chamber (AMC) reflector ~3.5 km below the seafloor (bsf) [*Singh et al*., 2006; *Combier*, 2007] and the presence of a mantle Bouguer anomaly bull's-eye at the segment center provide evidence for focused melt delivery and thickened crust near the segment center [*Detrick et al*., 1995; *Thibaud et al*., 1998].

Two 3-D tomography models of the segment made using airgun shots to OBSs reveal two low-velocity zones (LVZs) within the axial valley: a shallow LVZ above the AMC (~3.5 km bsf), which may correspond to high-porosity volcanic formations [*Seher et al*., 2010a], and a deep LVZ beneath the AMC, which may contain partial

Figure 1. Bathymetric maps of the Lucky Strike segment with important features of the seafloor. (a) Regional bathymetric map of the Lucky Strike segment with the central volcano in the middle of the axial valley. (b) Selected portion of the ridge segment with illumination along the ridge axis. The black lines show the extent of the main faults; WBF and EBF, respectively, western and eastern bounding faults. The yellow lines indicate the three-sumittal volcanic edifices (S: southern, NE: northeastern, and NW: northwestern volcanic cones) and the western volcanic ridge (WVR). Red circles over the volcano mark the hydrothermal vents. (c) Same area but with illumination across the ridge axis. The black rectangle in Figure 1a marks the extent of the figures presented in Figures 1b and 1c; the inset shows the location of the Lucky Strike segment on the MAR. Green lines mark the unrifted backsides of some rifted seamounts, the orange lines mark the extent of the Axial Magma Chamber (AMC) [*Combier*, 2007], the dashed magenta lines bound the neovolcanic zone [*Scheirer et al*., 2000], and the black rectangle shows the extent of the SISMOMAR 3-D survey. The blue lines mark the extent of the Figures 8–10. The blue circles show the limits of the vertical sections presented on Figure 5. The dashed gray lines correspond to the depth contours 1.68 and 1.9 km and highlight the extent of the central volcano and of the summital volcanic features.

©2014. American Geophysical Union. All Rights Reserved.

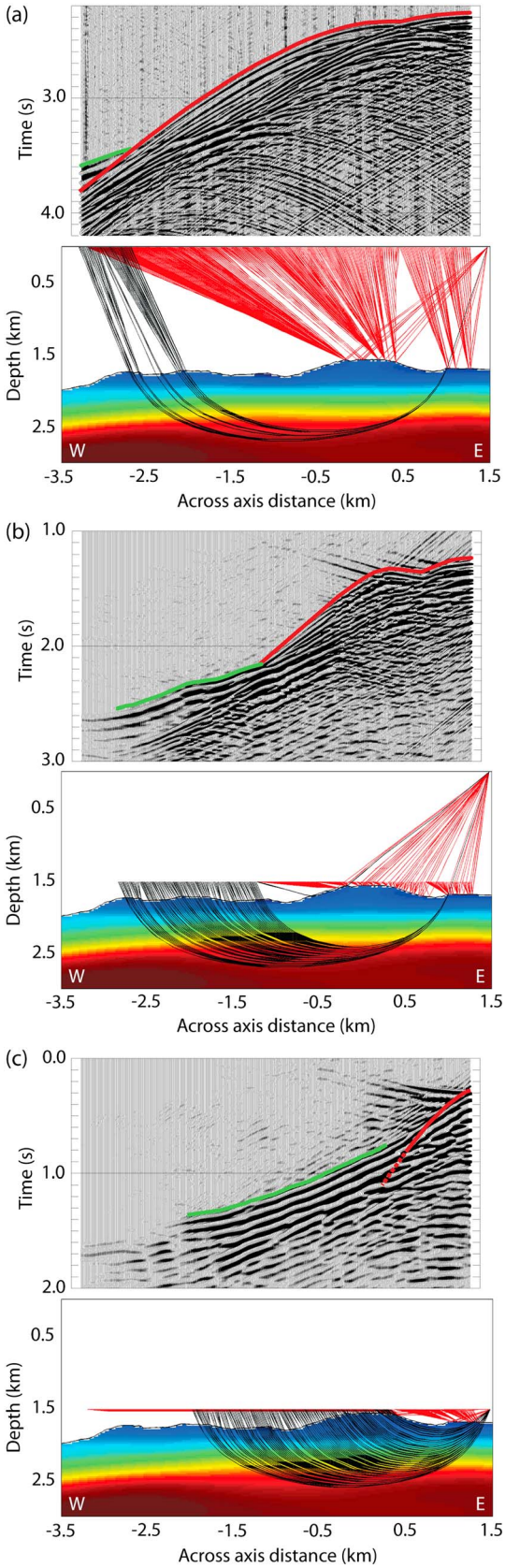

Figure 2

©2014. American Geophysical Union. All Rights Reserved.

melt [*Seher et al*., 2010b]. *Arnulf et al*. [2011] reprocessed the MCS data from the central volcano using a combination of SOBE and 3-D travel time tomography, and proposed that the porosity boundary between the relatively low-porosity lava lake and the surrounding high-vesicularity volcanic cones could act as a preferential pathway for the up-going hydrothermal flow. Subsequently, *Arnulf et al*. [2012] combined a SOBE approach with full waveform inversion to obtain a high-resolution (~50 m in spatial resolution) *P* wave velocity structure of layer 2A of the upper oceanic crust along one selected MCS profile and suggested that the young shallow crust beneath the Lucky Strike Volcano is formed from a stack of volcanic sequences emplaced within the axial valley.

For young crust, seismic layer 2 is commonly divided into two sublayers (2A and 2B) that have velocities ranging between ~2.2–5.0 km/s and ~5.0–6.0 km/s, respectively, and are delimited by a transition zone with steep velocity gradient ($>3\,s^{-1}$) at the base of layer 2A, which produces a strong reflector on seismic reflection images [e.g., *Harding et al*., 1993; *Vera and Diebold*, 1994]. For decades, the origin of the velocity transition at the base of layer 2A has been interpreted either as the lithological boundary between extrusives and sheeted dike complex [*Toomey et al*., 1990; *Harding et al*., 1993] or as a porosity limit within the extrusive section associated with an hydrothermal alteration front or a fracture front [*McClain et al*., 1985; *Burnett et al*., 1989; *Wilcock et al*., 1992; *Christeson et al*., 2007]. At Lucky Strike, *Arnulf et al*. [2011] further subdivided layer 2A of the central volcano into 2Aa and 2Ab since, in reprocessed reflection data, they imaged a new shallow reflector lying at 100–250 m below the seafloor, distinct from the usual strong layer 2A reflector at depth. This layer 2Aa reflector was most clearly seen beneath the volcano summital edifices, and *Arnulf et al*. [2011] suggested that it might correspond to the boundary between lava sequences of different ages. The deeper, conventional layer 2A event was relabeled 2Ab.

3. Data and Methods

Although multichannel streamer data have been previously used in tomographic studies to constrain the velocity structure of the Corinth rift [*Zelt et al*., 2004] or to shed light on the complexity of oceanic crust at different locations on the Mid-Atlantic Ridge [*Canales et al*., 2008; *Xu et al*., 2009], here we present an augmented two-step methodology developed to create enhanced 3-D velocity models by first redatuming streamer data to the seafloor using the SOBE method, followed by first-arrival travel time tomography of emergent phases. The framework of this method was originally presented by *Harding et al*. [2007], with extensions to 3-D outlined by *Arnulf et al*. [2011].

3.1. Data Acquisition

The Seismic Study for Monitoring of the Mid-Atlantic Ridge (SISMOMAR) seismic experiment was conducted along the Lucky Strike segment in the summer of 2005 onboard the French RV *L'Atalante*. The experiment included two key parts: (1) a segment-scale OBS-based 3-D tomographic experiment consisting of a 50 km by 50 km grid of 10,403 sea surface air gun shots to a 32 × 26 km array of 25 OBSs, centered on Lucky Strike Volcano [*Seher et al*., 2010b], and (2) a 3-D MCS experiment spanning the volcano consisting of 39 sail lines, each 18.5 km in length, spaced 100 m apart and recorded by a smaller array of 18 OBSs [*Seher et al*., 2010a]. For both objectives, a 360-channel, 4.5 km long digital hydrophone streamer with hydrophone group spacing of 12.5 m was towed at a nominal depth of 14 m. The source was a tuned, 18-element air gun array with a total capacity of 42.5 L (2594 in^3), fired every ~37.5 m during the 3-D experiment and every ~50 m during the segment-scale experiment. A total of 19,942 shots were fired during the 3-D MCS experiment, and data were recorded in 11 s long records sampled every 2 ms. Positions of receivers and sources were derived from shipboard and tail buoy GPS receivers and from 16 compass birds placed every 300 m along the streamer.

3.2. The Synthetic Ocean Bottom Experiment Method

During the SISMOMAR experiment, the hydrophone streamer recorded subseafloor reflections from seismic layer 2A (Figure 2a) and the AMC [*Singh et al*., 2006], as well as far offset subseafloor refraction events.

Figure 2. Synthetic Ocean Bottom Experiment (SOBE) method. (a) Representative shot gather recorded on the surface from line 14 with the corresponding arrivals and raypaths. (b) Same shot gather after downward extrapolation of the receivers to a horizon just above the seafloor, and (c) after downward extrapolation of the source and receivers. Red lines indicate the seafloor reflection arrivals while green lines and black raypaths denote the first arrival crustal refractions.

©2014. American Geophysical Union. All Rights Reserved.

However, most crustal refractions arrived behind the strong seafloor reflection at all but the farthest offsets and thus cannot be used in any straightforward manner to constrain uppermost crustal velocities. To overcome this limitation, we apply the SOBE method [*Harding et al*., 2007; *Arnulf et al*., 2011; *Henig et al*., 2012] to downward continue or redatum [*Berryhill*, 1984] sources and receivers from the 3-D experiment to a depth close to the seafloor.

The SOBE approach is an application of downward continuation [*Berryhill*, 1984] that transforms seismic sources and receivers to a level at (conformal) or near (flat) the seafloor, simulating an on-bottom refraction experiment using sea surface MCS data. It essentially unwraps the layer 2A/2B triplication, moving the refracted energy in front of the seafloor reflection (Figures 2b and 2c). This downward continuation closely replicates an on-bottom experiment such as near-bottom refraction experiment (NOBEL) [*Christeson et al*., 1994], but with orders of magnitude greater sampling. Using this method, the shallow crust can be explored with unprecedented coverage, including a multitude of crossing raypaths not found in conventional OBS refraction experiments.

Downward continuation or wave-equation datuming can be implemented in different ways: (1) using the Kirchhoff integral [*Berryhill*, 1979, 1984, 1986], (2) using a phase-shift approach [*Gazdag*, 1978], or (3) using a finite difference solution of the wave equation. Downward extrapolation is a type of migration algorithm, and the trade-offs between the different approaches are extensively presented in the related literature.

In this study, the downward continuation of both shots and receivers from streamer data to a flat datum close to the seafloor was implemented using a prestack phase-shift approach. The wavefield was downward propagated in two steps. First, the receiver wavefield (360 traces) from each shot gather was extrapolated to a horizontal level just above the seafloor (Figure 2b). Then, after sorting the data into a common receiver location space and recognizing source-receiver reciprocity, each source wavefield (120 shots per common receiver location gather) was extrapolated to the same depth (Figure 2c). To minimize aliasing, filtering was applied prior to each phase-shift extrapolation step in the FK domain. To minimize edge effects, the first 12 and last 12 traces were tapered using a sinusoidal weighting operator. Prior to the first extrapolation, the direct wave was muted from the data in the time-offset domain. Finally, after extrapolation, the data were reorganized back into shot gathers, and clear, emergent refracted arrivals were present at ranges 0.5–4.0 km as compared to 4.0–4.5 km on the original surface gather. The extent of the extrapolated arrivals depends on the distance between the extrapolation datum and the seafloor, the underlying velocity function, and local topography; therefore, the source-receiver range of extrapolated first arrivals changes slightly from one location to another.

3.3. Streamer Traveltime Tomography

Within the SISMOMAR 3-D experiment, up to ~7 million source-receiver pairs were recorded. An important question for such a large MCS data set is when does the gain in model resolution from picking more arrivals reach the point of diminishing returns and simply take more time with little gain. To reduce the size of this data volume, only every fifth shot (~every 190 m) along each of the thirty-nine 100 m spaced lines was inverted. When counting source-receiver pairs with usable refracted arrivals, about 8% of all total pairs were used in the inversion. The decimation of the source-receiver pairs was justified by the fact that the data set, in some sense, laterally oversamples beyond the resolution that can be obtained from conventional traveltime tomography (covered more fully in Appendix A1). Even so this is a large data set and in order to speed up and increase the accuracy and consistency of picking, a semiautomatic tool that combined waveform cross-correlation and cluster analysis [*Sigloch and Nolet*, 2006] was used. Also, to improve the efficiency of the 3-D inversion (i.e., reaching the global minimum), we needed the starting 3-D model to be as close as possible to the final structure.

To this end, first arrivals from every downward continued, fifth shot were picked and inverted for using source-receiver ranges extending between 0.5 and 4.0 km. To control the picking consistency along a given line, picks from the preceding shot were used to guide the current one. Initially, 10 equidistant 2-D profiles were analyzed and inverted starting from a 1-D velocity model attached beneath a 2-D seafloor (Figure S1a in the supporting information). These 10 equidistant 2-D velocity models were then interpolated to generate an initial 3-D velocity cube. Using this interpolated velocity volume, predicted first arrival times for all remaining source-receiver pairs were calculated for the remaining 29, interleaved seismic lines. Approximately 560,000

©2014. American Geophysical Union. All Rights Reserved.

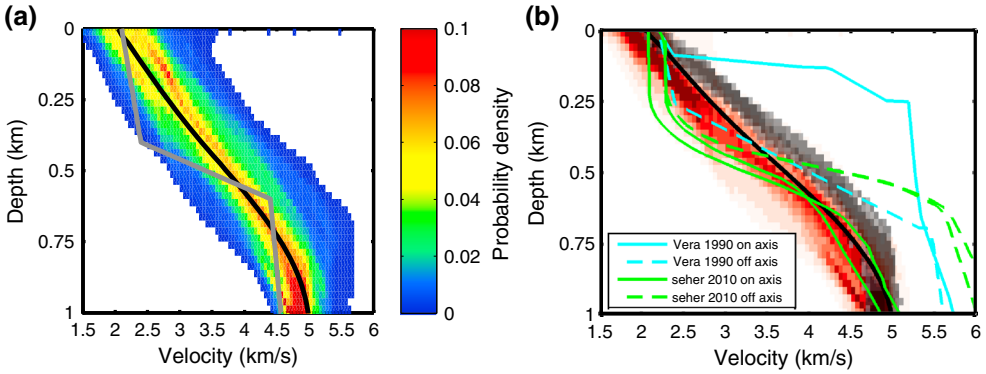

Figure 3. (a) Velocity probability density functions for the center of the Lucky Strike segment computed at each depth below the seafloor. The colormap corresponds to the velocity probability density functions for the final 3-D model, the gray line shows the starting velocity model for the first 10 2-D tomography inversions. (b) Velocity probability functions computed, respectively, within the central volcano (red colormap) and beyond the eastern boundary fault between 6 and 8 km distance across axis (gray colormap). Green lines correspond to on- and off-axis velocities for Lucky Strike from *Seher et al*. [2010c] and cyan lines correspond to on and off-axis velocities for the EPR at 9 N *Vera et al*. [1990]. The black line on Figures 3a and 3b show the average velocity profile from our best fitting model.

arrival times from ~3400 shots were then picked quasi-automatically using a combination of waveform cross-correlation and cluster analysis [*Sigloch and Nolet*, 2006] on the set of predicted and existing picks (Figure S1b). During the cross-correlation step, the predicted picks for the current line were adjusted slightly so as to be consistent with existing picks. The 29 remaining seismic lines were then inverted in 2-D using starting models extracted from the initial 3-D velocity cube (Figure S1c). A new 3-D interpolated volume was created from the 39 best 2-D velocity models and used as the basis for the full 3-D traveltime inversion, reducing the number of 3-D iterations and thus the computational cost (Figure S1d).

The 2-D and 3-D velocity models were calculated using an updated version of the traveltime tomography code of *Van Avendonk et al*. [2004] suitable for the downward continued geometry that reduces traveltime errors associated with the discretization of the seafloor bathymetry. The velocities for the 39 2-D seismic lines were discretized on a 32 km long by 4 km deep model with 25 m grid spacing. The forward problem (ray tracing and traveltime calculation) was solved using a shortest path method [*Moser*, 1991]. Regularization was achieved by minimizing a cost function that penalizes a combination of data misfit (data residuals weighted by their uncertainties) and model roughness. We identified six sources of uncertainty in the traveltimes: (1) the uncertainty related to the shot location (~2 ms), (2) the uncertainty related to the receiver location (~2 ms), (3) the uncertainty related to the bathymetry (~7 ms), (4) the uncertainty related to the SOBE method (~5 ms), (5) the uncertainty related to the seismic ray tracing for shallow crustal *Pg* waves (~7 ms), and (6) the uncertainty of the traveltime picks themselves (~5 ms). We estimated the overall uncertainty (~12 ms) as the square root of the sum of the individual variances. The roughness operator was chosen to penalize the first and second derivatives of the velocity model.

In order to achieve the best fit in the 3-D inversion, the same parameters were used except that about 1% of the data were trimmed due to extreme misfit and the roughness operator penalized the second derivatives of the velocity model only. The subsurface velocity volume was 32 km long by 5 km wide by 3 km deep, and discretized on a 25 m regular grid.

3.4. Seismic Reflection Imaging

The first 25 traces of the downward continued seismic lines were sorted into common midpoint gathers (CMP) and stacked to produce seismic reflection images of the central volcano. A normal moveout velocity of 1.5 km/s was applied down to 250–300 m below a smoothed seafloor with 2.2 km/s being used below that level. Seismic sections from lines 15, 24, and 39 are presented in the next section.

4. Results

4.1. Three-Dimensional Velocity Structure

Figure 3a shows the *P* wave velocity distribution within the best fitting 3-D tomographic model as a function of depth below the seafloor. A velocity variability of 1.5–2 km/s is observed at each depth below the seafloor. This variability is necessary to adequately fit the data in both the 2-D and 3-D inversions.

©2014. American Geophysical Union. All Rights Reserved.

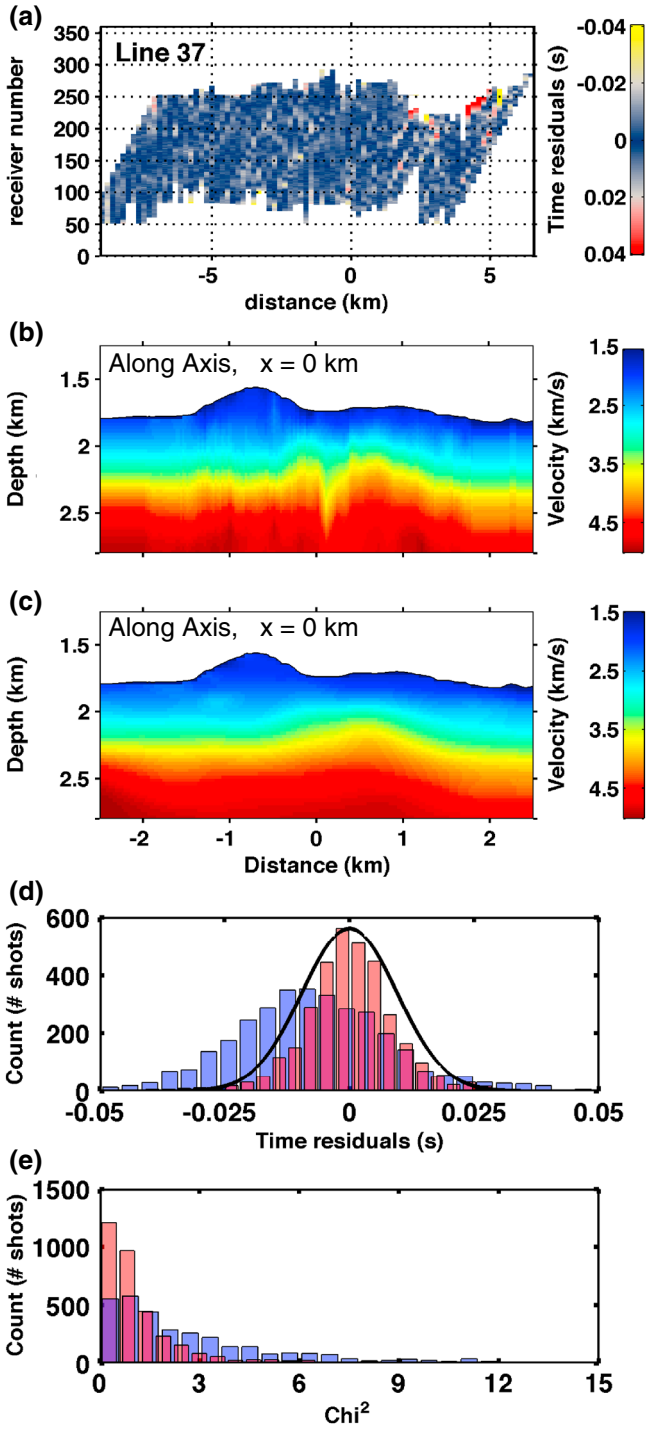

Figure 4. Traveltime residuals. (a) Residual traveltimes predicted by the final 2-D velocity model along seismic line 37 displayed as a function of across-axis location and source-receiver number. Receiver 1 is at 4.6675 km and Receiver 360 at 0.180 km offset. (b and c) Along-axis velocity sections at 0 km across axis from the initial and final 3-D velocity models, respectively. Distribution of the (d) traveltime residuals and (e) of chi-square for the starting (blue colormap) and final (red colormap) 3-D models. The black line corresponds to a Gaussian distribution with a zero mean and a standard deviation of 9.5 ms.

For the 10 initial 2-D models, traveltime residuals were reduced from ~64 ms to ~12 ms by the inversion (Figure S1a). The models for the remaining 29 profiles, being derived by 3-D interpolation, had lower initial traveltime residuals of 20–30 ms, but were ultimately fit to the same overall accuracy (~11 ms, Figure 4a—Line 37), which also corresponds to the estimated pick uncertainty. Moreover, Figure 4a illustrates the fact

©2014. American Geophysical Union. All Rights Reserved.

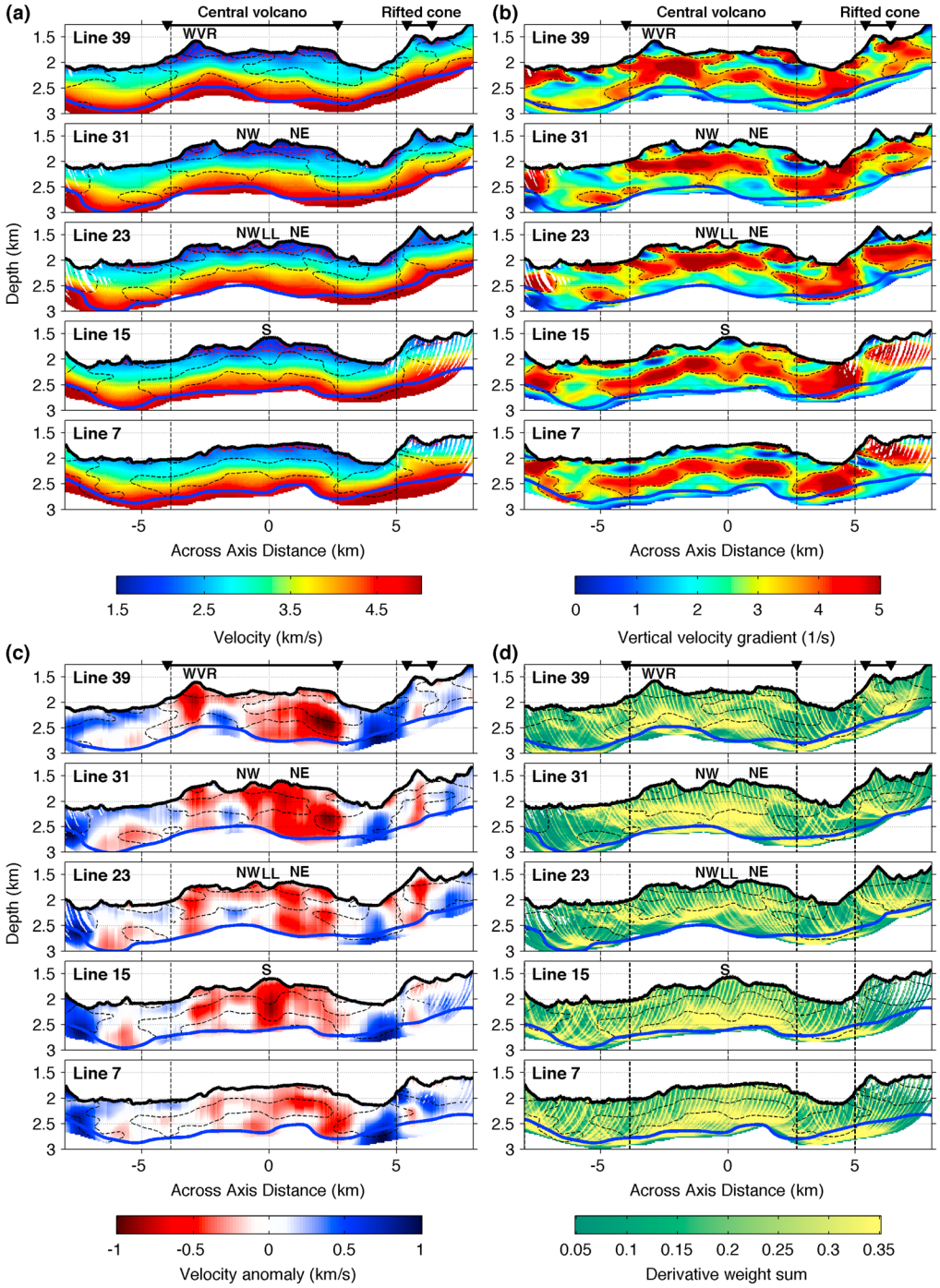

Figure 5. Upper crustal velocity structure of Lucky Strike Volcano. (a) Two-dimensional vertical slices of *P* wave velocity for seismic lines 7, 15, 23, 31, and 39. (b) Corresponding vertical velocity gradient sections. (c) Velocity anomaly sections. The one-dimensional vertical velocity profile used to produce these anomaly sections is presented in Figure 3. (d) Derivative weight sums highlighting the excellent ray coverage. The blue lines are the 4.8 km/s velocity contour, a proxy for the top of layer 2B, and the dashed black lines contour the 3.5 s^{-1} vertical velocity gradient. Vertical black dashed lines delimit three regions of interest: the central volcano, the central valley, and the eastern crust beyond the axial valley. S: southern, NE: northeastern, and NW: northwestern volcanic cones; WVR: western volcanic ridge and LL: lava lake locations.

that the data are equally well fit across nearly all source-receiver pairs with few coherent trends in the residuals. These residuals are evidence that the preferred 2-D models capture a significant part of the overall complexity (i.e., small-scale crustal heterogeneities) within the shallow crust underneath the Lucky Strike Volcano.

©2014. American Geophysical Union. All Rights Reserved.

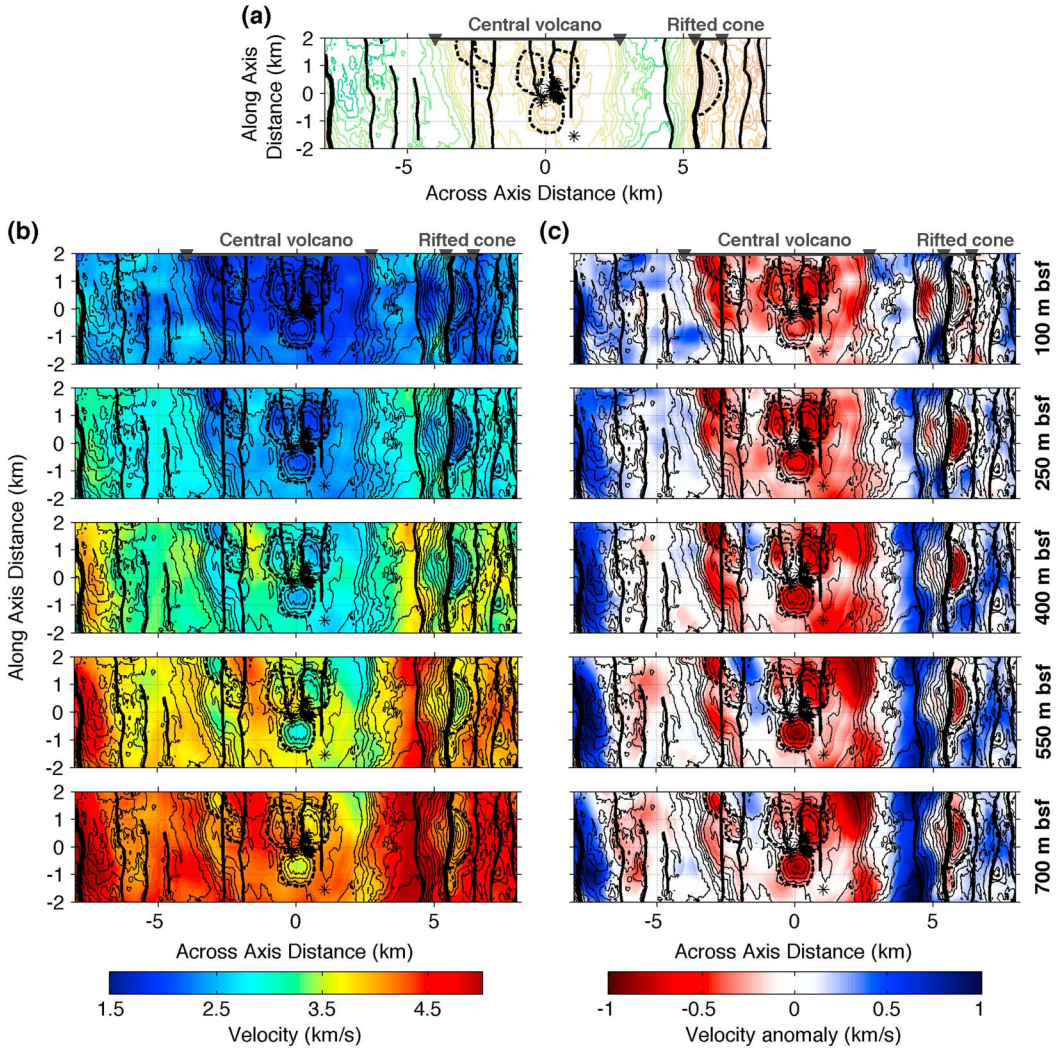

Figure 6. Horizontal velocity slices at depths of 0.1, 0.25, 0.4, 0.55, and 0.7 km below seafloor (bsf). (a) Local bathymetric map with important features of the seafloor (see Figure 1). The black lines mark significant faults, the dashed black lines outline different volcanic edifices and the black stars mark the hydrothermal vents. (b) Velocity. (c) Velocity anomaly sections.

The MCS profiles from the SISMOMAR 3-D experiment were shot across axis because the geology suggests that this is closest to a dip direction, thus minimizing out of plane propagation. However, the composite 3-D model constructed from the individual 2-D model will inevitably end up being rougher than necessary in the third direction, particularly in regions of greatest seafloor roughness. By inverting this data set explicitly as a 3-D cube, we obtain a model smoothed in all directions, one that can more readily be used to explore crustal processes. One potential advantage of a 3-D inversion is that it can correctly account for energy that propagates outside of the source-receiver plane, but this advantage is mitigated by the reliance of the downward continuation step on 2-D propagation. Nevertheless, the 3-D inversion improves model smoothness in the along-axis direction and allows us to identify unresolved 3-D structure from local increases in the residuals. The along-axis velocity section shown in Figures 4b and 4c, which cuts the southern volcanic cone and lava lake, highlights the difference between the composite 3-D model formed from 2-D models ("starting model"), and the result obtained with the full 3-D inversion. The 3-D inversion removes the velocity artifact observed at ~0.25 km distance along-axis underneath the lava lake that could otherwise be misinterpreted. Overall the traveltime residuals of the preferred 3-D model follow a quasi Gaussian distribution with a zero mean and a standard deviation of 9.5 ms, Figures 4d and 4e. The uniformly low misfit across profiles also indicates that our preferred 3-D model has captured the majority of the 3-D structure.

©2014. American Geophysical Union. All Rights Reserved.

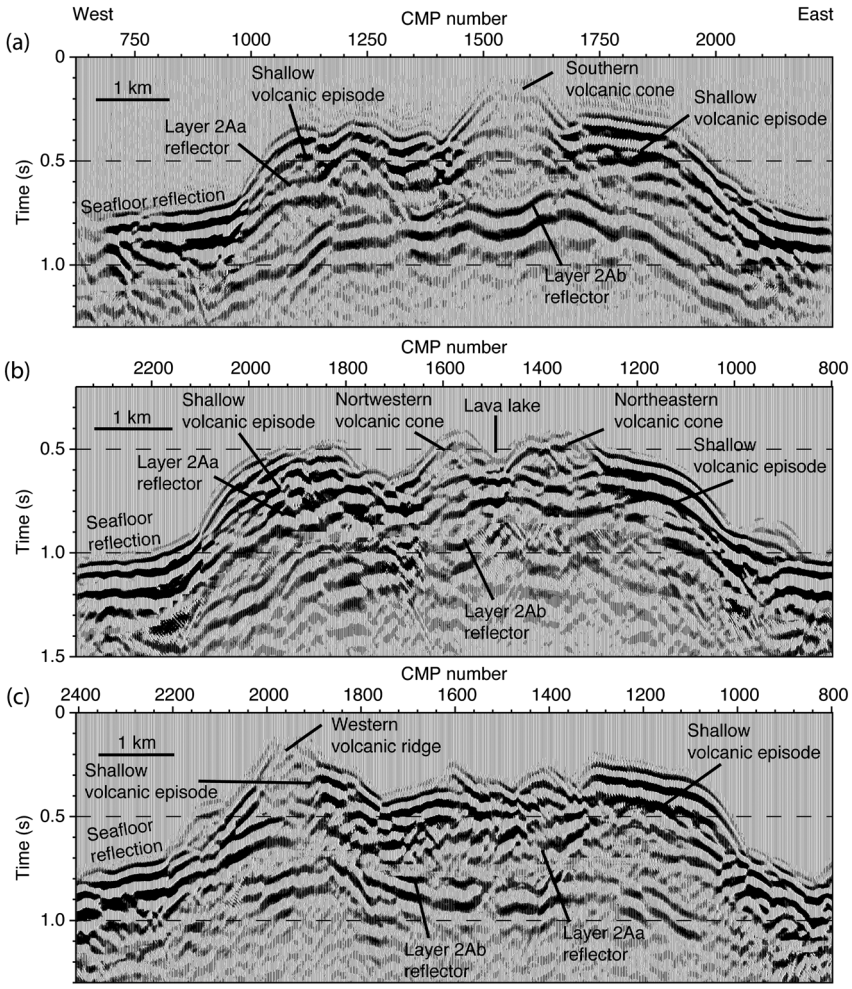

Figure 7. Stacked seismic sections of the shallow crust for (a) line 15, (b) line 24, and (c) line 39 produced from the downward extrapolated data. Only the first 25 traces of each CDP gather were used to produce these stack sections. The average along-axis location of these seismic lines is, respectively, −0.6, 0.3, and 1.8 km.

The most common way to define the seismic layer 2A/2B boundary, inherited from 1-D velocity modeling, is to pick "by eye" a bend in the vertical velocity profile corresponding to a significant drop in the velocity gradient [*Harding et al*., 1989; *Vera et al*., 1990; *Harding et al*., 1993; *Christeson et al*., 1996; *Hussenoeder et al*., 2002a; *Seher et al*., 2010c]. Employing this method on the probability density function of all 1-D models extracted from the 3-D volume, indicates that the base of the layer 2A is typically at depths of ~0.7–0.85 km (Figure 3a). Another approach is to note that the base of the layer 2A also appears to be highly correlated with the velocity horizon of 4.8 ± 0.15 km/s and so this velocity could be used as a proxy for determining the depth of the layer 2A/2B boundary. However, neither picking the average depth where the velocity gradient drops nor using a constant velocity horizon can provide a universal rule for the base of the layer 2A in a complex 3-D structure such as Lucky Strike Volcano. In this study, the combination of a SOBE method and 3-D traveltime tomography has allowed, for the first time, the construction of a tomography structure of the upper oceanic crust with enough spatial resolution (~200 m vertically and ~500 m laterally, see Appendix A1) to image the high-velocity gradient region at the base of layer 2A ($>3\,s^{-1}$). In the following analysis of Lucky Strike Volcano's velocity structure, we define the base of layer 2A using this high-velocity gradient region.

The region sampled by our 3-D tomographic experiment includes the Lucky Strike Volcano, the surrounding median valley, the eastern bounding wall and part of the western bounding wall, from the seafloor to a depth ~1 km bsf. Vertical and horizontal slices from the resulting 3-D velocity cube are shown in Figures 5 and 6. Ray

©2014. American Geophysical Union. All Rights Reserved.

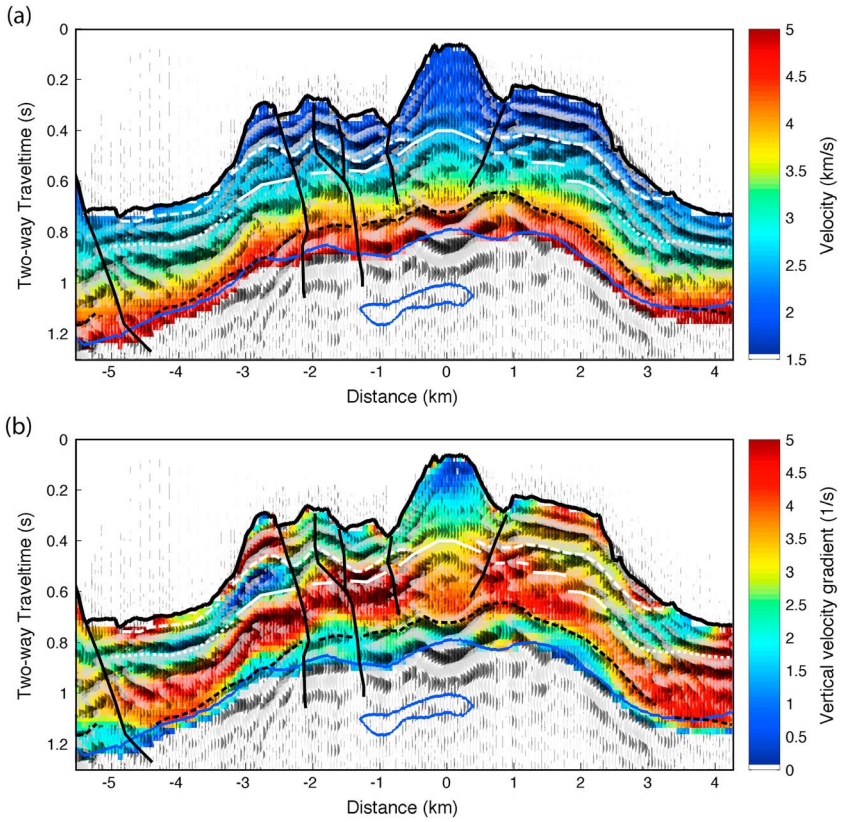

Figure 8. Seismic reflection and refraction results from line 15 (−0.6 km along-axis distance). (a) Seismic reflection section superimposed on the tomography velocity model converted from depth to two-way traveltime. (b) Combined seismic reflection and vertical velocity gradient sections. Dashed black lines correspond to the layer 2Ab reflection, solid white lines mark the layer 2Aa reflection, and dotted white lines indicate the possible continuation of the Layer 2Aa reflector within the median valley based only on the vertical velocity gradient. Dashed white lines correspond to the base of shallow volcanic sequences and black lines mark interpreted faults.

coverage was densely distributed over most of the model but was enhanced near the layer 2A/2B boundary (Figure 5d).

Overall, our tomographic model reveals velocities that are everywhere slower than 5.7 km/s in the upper 1 km (Figures 3a, 5a, and 6b). Vertical depth sections reveal a ~200–300 m thick zone of high-vertical velocity gradient ($> 3\,s^{-1}$) (Figure 5b) corresponding to the base of layer 2A [*Arnulf et al.*, 2011]. To bring out some of the strong lateral velocity variations, the average 1-D velocity was subtracted from our best fitting model to create anomaly maps and sections (Figures 5c and 6c). Broadly, velocities are low within the central volcano, average in the median valley, and high beyond the bounding faults (Figure 3b), but in detail the behavior is more complex. For the purposes of further discussion the seismic structure will be divided into three different zones: (1) the median valley which surrounds the central volcano (−8 km to −3.85 km and 2.7 km to 5 km across axis), (2) the central volcano (between −3.85 km and 2.7 km across axis), and (3) the eastern crust beyond the axial valley (5–8 km across axis).

Within the median valley, our tomography model reveals velocities typical of young layer 2A [*Harding et al.*, 1989; *Christeson et al.*, 1994; *Hussenoeder et al.*, 2002b], ranging from 2.2 km/s at the seafloor to ~4.8 km/s at the base of the transition region; the highest velocities (4.9 ± 0.2 km/s) being observed within upper layer 2B (Figures 5a and 6b). Along-axis, the seismic structure appears to be laterally homogeneous and no strong velocity variations are noted. In this region, the base of layer 2A is well approximated by the 4.8 km/s velocity horizon (Figure 5b) and lies close to the base of our velocity structure, just above the region of elevated derivative weight sum that identifies where refractions from the top of layer 2B turn (Figure 5d). In the vicinity of the axial valley bounding faults, two elongated zones of anomalously high velocity (+0.4 to +1 km/s) are revealed (Figures 5c and 6c), in addition to an anomalously thin layer 2A (~400 m).

©2014. American Geophysical Union. All Rights Reserved.

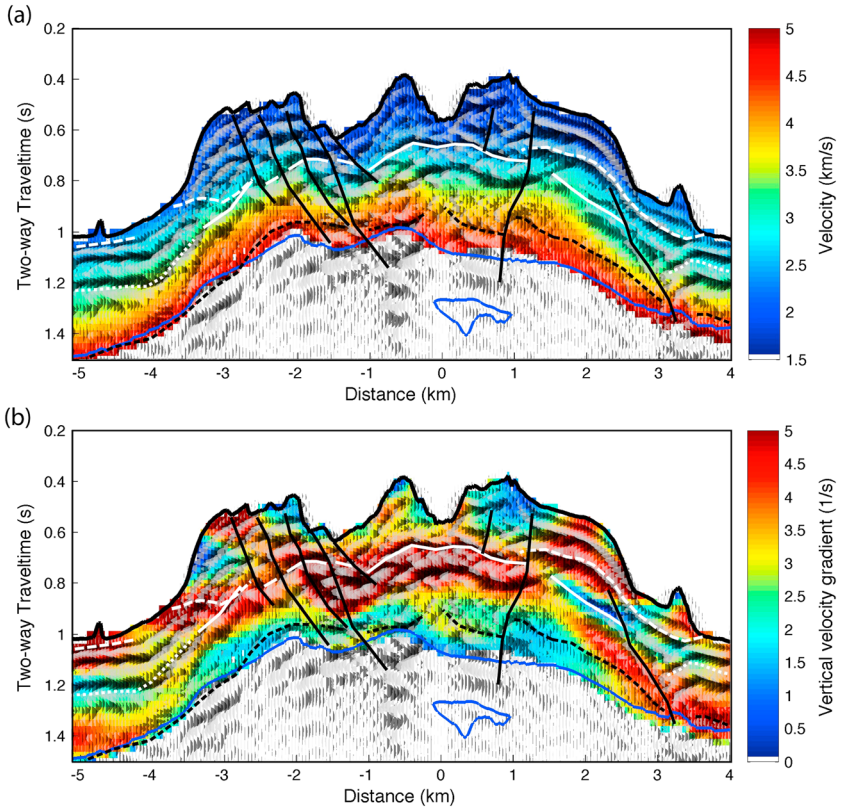

Figure 9. Same as Figure 8 for seismic line 24 (0.3 km along-axis distance).

In comparison to the typical layer 2A velocity structure observed beneath the median valley, maps, and slices through the central volcano reveal an anomalously low-velocity region (Figures 5c and 6c), with slight lateral changes in velocity structure. The layer 2A P-wave velocities are slower than those observed in the median valley and range between 1.7 km/s and ~4.75 km/s (Figures 3, 5a, and 6b). The base of the high vertical gradient zone in P-wave velocity has shoaled beneath the central volcano (Figure 5b). The transition between 2A and 2B is still imaged on the ray density sections since deeper refractions preferentially turn within the top of layer 2B (Figure 5d). Interestingly, this high-velocity gradient zone within layer 2A underlies a shallow and quite uniform low-velocity region that extends throughout the central volcano (see Figures 5c and 6c—depths slices 100 m and 250 m). Nevertheless, some strong lateral and vertical velocity variations are present within the central volcano. Indeed, narrow pipelike zones of lower velocities are found below the three volcanic cones, extending to the bottom of our model (Figures 5c and 6c). The extended anomalies are much stronger beneath the southern and northwestern volcanic edifices, being similar in magnitude to the velocity anomaly of the western volcanic ridge (Figures 5c—Line 39 and 6c). However, extremely low velocities (1.8 to 2.2 km/s) are observed underneath all the volcanic mounds down to 300 m bsf, in contrast to the typical velocities ($>$ 2.2 km/s) [*Harding et al*., 1989; *Christeson et al*., 1994; *Hussenoeder et al*., 2002b] present within the surrounding region and beneath the lava lake (Figures 5c and 6b). Furthermore, a deep low-velocity unit is observed on the northeastern side of the central volcano (Figures 5c and 6c). This last observation is consistent with previous OBS tomography results reported by *Seher et al*. [2010a].

The crustal velocities within the eastern wall of the axial valley (off axis) shows a thinner ~500 m and fairly homogeneous layer 2A except beneath the topographic high at 5.75 km across axis (Figures 5 and 6). Below this mound, a low-velocity region is observed and the high-velocity gradient is pulled away from the base of the model, echoing the behavior beneath the central volcano. Furthermore, based upon the velocity anomaly slices (Figures 5c and 6c) and local velocity distributions (Figure 3b) layer 2A and 2B velocities are measurably faster off axis. Across axis, a velocity increase of 0.5–0.8 km/s is observed within layer 2A, while a slight increase from ~4.75 km/s to ~4.95 km/s is found within the shallowest part of layer 2B (Figures 3b, 5c, and 6c).

©2014. American Geophysical Union. All Rights Reserved.

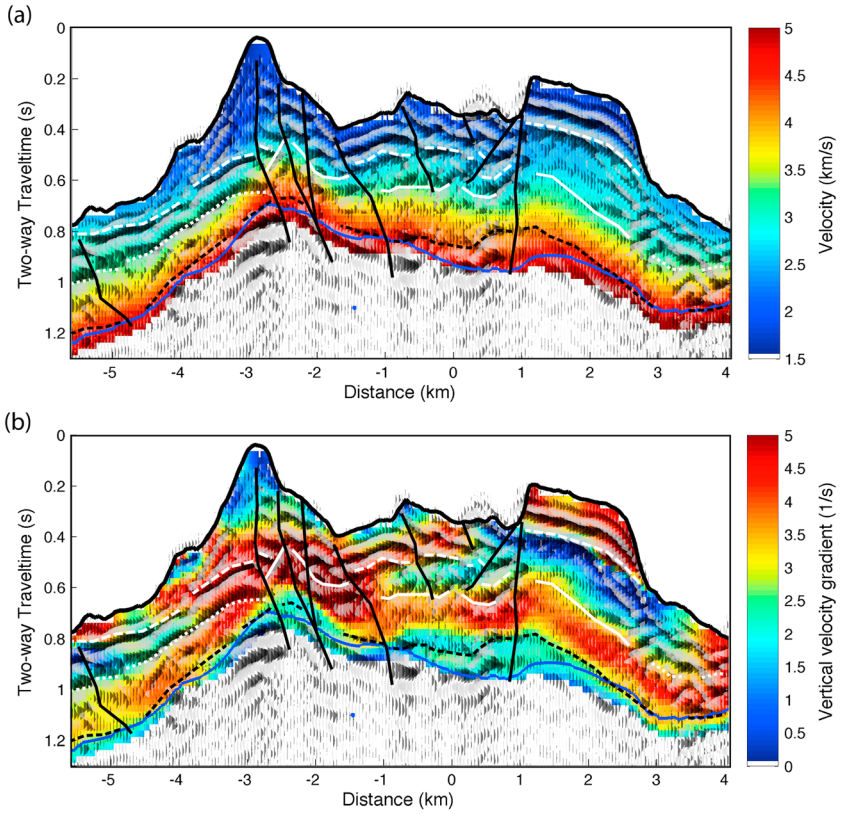

Figure 10. Same as Figure 8 for seismic line 39 (1.8 km along-axis distance).

4.2. Combined Seismic Reflection/Refraction Imaging

Traditionally, traveltime tomography methods oversmooth the vertical and horizontal velocity structure of the upper crust, whereas conventional multichannel seismic (MCS) processing highlights impedance contrasts while yielding little direct information on velocity. The conventional reflection and refraction methods thus provide complementary but incomplete images of the oceanic crust, and a joint analysis of both methodologies can lead to a better interpretation of seismic images.

Figure 7 shows that in addition to the strong layer 2A reflector at depth (marking the transition between layer 2A and B), there is a shallower reflector imaged at 100–350 m (0.1–0.45 s below the seafloor (bsf)), which *Arnulf et al.* [2011] recognized as originating from the top of the region of high-vertical velocity gradient and termed the layer 2Aa reflector. This reflector is nearly ubiquitous beneath the central volcano and is distinct from the conventional layer 2A reflector, which, following *Arnulf et al.* [2011] relabeled, reflector 2Ab. Beyond the central volcano, within the median valley, the continuity of the layer 2Aa reflector can only be inferred using the vertical velocity gradient sections (Figures 8b, 9b, and 10b) because, on the seismic reflection sections, the corresponding reflection is either absent or merged with the seafloor arrival. The distribution of the layer 2Aa reflector within the oceanic crust at slow spreading ridges is, as yet, unknown. Even at fast-spreading ridges a double step transition to layer 2A is reported in some areas (e.g., 9°N [*Vera et al.*, 1990; *Christeson et al.*, 1994] and 17° S [*Hussenoeder et al.*, 2002b]) but not others, although this may represent, in part, an analysis bias that will lessen as techniques improve. Furthermore, within the central volcano several low-frequency and laterally continuous reflections are imaged at depths less than 150 m below the seafloor reflection ($<$0.2 s bsf). These shallow reflectors are further characterized by their own distinct high-velocity gradient zones (Figures 8, 9, and 10) and separate the extremely low-velocity lava regions (1.8–2.2 km/s) from the more typical basaltic crust below ($>$2.2 km/s). Interestingly, these shallow volcanic layering also appear to be nearly ubiquitous across the central volcano, where the final 3-D tomographic model reveals extremely low velocities (Figures 8a, 9a, and 10a).

In general, the layer 2Ab reflection originates from the bottom of the high-velocity gradient layer that forms the lower limit of layer 2A, except beneath the lava lake and surrounding volcanic mounds. For example, on

©2014. American Geophysical Union. All Rights Reserved.

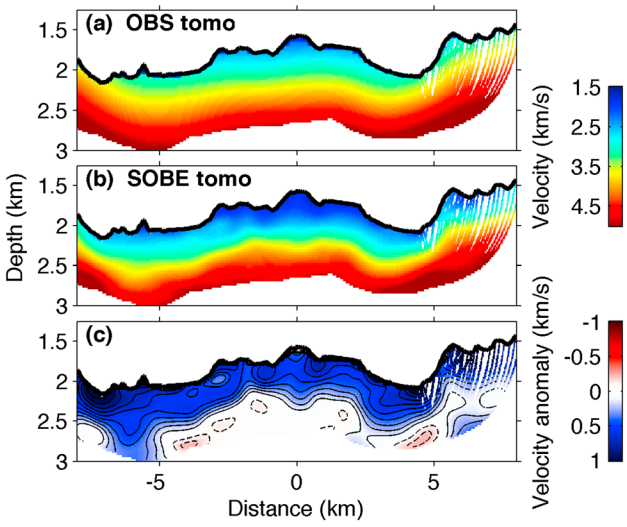

Figure 11. SOBE and OBS tomography model [*Seher et al.*, 2010a] compared along seismic line 14. Only the upper crust that is recovered by the SOBE method is shown and compared. (a) OBS velocity model. (b) SOBE velocity model. (c) Velocity difference computed by subtracting the SOBE velocity model from the OBS velocity model.

the seismic line 24, Figure 9, there is a ~0.2 s discrepancy between the base of the high gradients and the layer 2Ab reflection. In fact, beneath the lava lake and the surrounding volcanic mounds, the highest-velocity gradients within layer 2A produce the 2Aa reflection and it is a second high-velocity gradient layer of smaller amplitude (~3 s^{-1}) that marks the transition between the layers 2A and 2B. Finally, one can notice a significant drop in the seafloor reflection amplitude at the three volcanic cones and at the northwestern volcanic ridge (Figure 7). This drop in the seismic impedance contrast is consistent with the lower velocities imaged by the tomographic inversions.

To summarize, the shallow crust beneath the Lucky Strike Volcano presents three distinct seismic velocity units delimited by the layer 2Aa and 2Ab reflectors, respectively. From seafloor depth down to the layer 2Aa reflector, there is a 250–350 m low-velocity layer (<3.0 km/s) composed of several distinct sequences. It overlies a 300–350 m thick high-velocity gradient zone delimited, respectively, by the layer 2Aa and 2Ab reflectors, except beneath the lava lake where an extra high-velocity gradient layer, underlying the main high-velocity gradient layer, marks the transition between 2A and 2B. Within this layer, velocities increase rapidly from ~3.0 km/s to ~4.5 km/s. At the base of this high-velocity gradient zone, the layer 2Ab reflector marks the transition between layer 2A and B.

5. Discussion

5.1. Comparison With Previous Ocean Bottom Seismometer Tomography

During the SISMOMAR experiment, seismic refraction data were also acquired by an array of 18 ocean bottom seismometers (OBSs) deployed in an 18×10 km^2 box around the central volcano. The source array was the same as for the seismic reflection experiment and the refraction data were analyzed by *Seher et al.* [2010a]. A low-velocity region within the median valley, and a low-velocity anomaly underneath the central volcano were discovered (Figure 11a). However, the OBS tomography model captures only the larger wavelength features with reduced amplitude. Furthermore, the OBS tomographic model seems to be only moderately constrained, at best, at shallow depths (<600–800 m) within the central volcano, with vertical smearing likely to greater depths. In contrast, the SOBE results suggest that the upper low-velocity anomaly is confined to the upper 500 m of the crust (Figure 11b). The combination of a SOBE method, with its artificial near-seafloor geometry, and 3-D traveltime tomography produces velocity models with horizontal and vertical resolutions of hundred of meters that are beyond the reach of conventional OBSs experiments with deployments on a 5 km grid. Moreover, if we take the current SOBE model as reference (Figure 11c), we can examine the errors within the OBS model. In fact, the largest systematic error in the OBS model is the lack of vertical resolution in the upper ~600 m of crust (Figure 11c). At shallow depths <600 m bsf, the crustal velocities given by the SOBE

©2014. American Geophysical Union. All Rights Reserved.

model (Figure 11a) are 0.4–1.0 km/s lower than the velocities given by the OBS tomography (Figures 11b and 11c). The OBS-based traveltime tomography inversion method overestimates velocities at shallow depths as a result of the lack of turning rays and the smoothness regularization operator, which minimizes the curvature of the velocity model.

Therefore, by using a new methodology that combines a "Synthetic Ocean Bottom Experiment" geometry and 3-D traveltime tomography, our study produces significant improvements in tomographic imagery and spatial resolution (see Appendix A1). Interpretation of the 3-D model in conjunction with MCS profiles potentially provides new insights into the processes shaping upper crustal structure at slow spreading ridges.

5.2. Average Layer 2A and 2B Velocities Versus Age Versus Emplacement History

Numerous seismic surveys have been conducted to study the structure and creation of the oceanic crust at diverse locations on fast, intermediate and slow spreading ridges. A compilation of some representative results is presented in Figure 12a. The on-axis layer 2A thickness at fast-spreading ridges [*Harding et al*., 1993; *Hussenoeder et al*., 2002b] appears to be $<$275 m while the common velocity at the base of the layer 2A ranges between 5.2 and 5.5 km/s. In comparison, at intermediate [*Cudrak and Clowes*, 1993; *McDonald et al*., 1994; *Canales et al*., 2005] and slow spreading ridges [*Minshull et al*., 2003; *Hussenoeder et al*., 2002a; *Seher et al*., 2010c], the typical layer 2A thickness is 250–400 m and 375–750 m, respectively, while the basal velocity is 4.8–5.3 km/s and 4.6–5.0 km/s. From the previous results, the expected velocity of zero-age crust at the surface at all these spreading centers is ~2.1–2.6 km/s, although some back arc locations are even slower [*Jacobs et al*., 2007]. Overall, our velocity model is similar to those of *Minshull et al*. [2003] (MAR, 8–9°S) and *Seher et al*. [2010c] (Lucky Strike segment, MAR ~37.3°N) and yields velocities that are lower than the existing velocity compilation at slow spreading ridges [*White et al*., 1992; *Henig et al*., 2012, Figure 7]. In fact, the Lucky Strike area and the MAR between 8 and 9°S were chosen for study because they are two unusually shallow, hot spot-influenced segments. Thus, while layer 2A is unusually thick in these regions compared to other spreading rates, there is likely a selection bias: *Hussenoeder et al*. [2002a] gets smaller layer 2A thickness at the 35°N segment of the MAR with a small hot spot influence. One other notable difference is that a significant portion of our velocity model represents velocities lower than 2.2 km/s, which is below the expected velocity of zero-age oceanic crust. This can be attributed to the low-velocity constructional central volcano and more particularly to the extremely low-velocity, high-porosity summit volcanic mounds.

The layer 2B velocities from this study can be compared with previous studies of Lucky Strike [*Seher et al*., 2010c] and the OH-1 segment of the MAR at 35°N [*Hussenoeder et al*., 2002a; *Seher et al*., 2010c], both of which report 1-D velocity models based on analysis of selected gathers. *Seher et al*. [2010c] report pairs of on-axis and off-axis velocity models for an extended flow line MCS profile crossing the central volcano. On-axis, layer 2B velocities are, as expected, comparable to velocities reported here, but upper layer 2B velocities for ~2 Ma old crust on either side of the axis are ~5.6 km/s. This is significantly faster than the off-axis velocities found here of ~4.95 km/s for crust with a maximum age of ~0.8 Ma (Figure 3b). One possibility is simply that the increase in 2B velocity accelerates at ages beyond our study region. Alternatively, the off-axis measurements from *Seher et al*. [2010c] might be unrepresentative of the average upper 2B velocities. At present, the only systematic study of layer 2B velocities along flow lines is for the Juan de Fuca ridge and there systematic increases cease after 0.5 Ma although layer 2B velocities may still vary between 5 and 6 km/s in older crust [*Newman et al*., 2011]. For the OH-1 segment, *Hussenoeder et al*. [2002a] found upper layer 2B velocities around 5 km/s for crustal ages between 0 and 1.9 Ma with no apparent age trend. The outliers were a pair of models from a CMP profile collected on the eastern terrace of the segment over 0.7 Ma crust that had upper layer 2B velocities exceeding 6 km/s. Unlike the other profiles, the corresponding stacked section lacked a coherent layer 2A reflection suggesting it was indeed anomalous. There is no obvious anomalous structure along the profile examined by *Seher et al*. [2010c], even so, if *Newman et al*. [2011] is a guide then velocity variations this large may be expected on flow line profiles without any overall trend. The evolution of layer 2B velocities at the MAR warrants further study.

On the basis of a compilation of published seismic survey data, *Grevemeyer et al*. [1999] has shown that in crust $<$ 1 Ma old, seismic velocities within the layer 2A are commonly $<$ 3 km/s. Moreover, they found that velocities rise rapidly to a typical value of mature oceanic crust (~4.3 km/s), nearly doubling in 8–10 Ma and remaining essentially unchanged thereafter. *Carlson* [2004] augmented the *Grevemeyer et al*. [1999] study and proposed a simple model to account for the layer 2A velocity versus age, based upon an asperity

©2014. American Geophysical Union. All Rights Reserved.

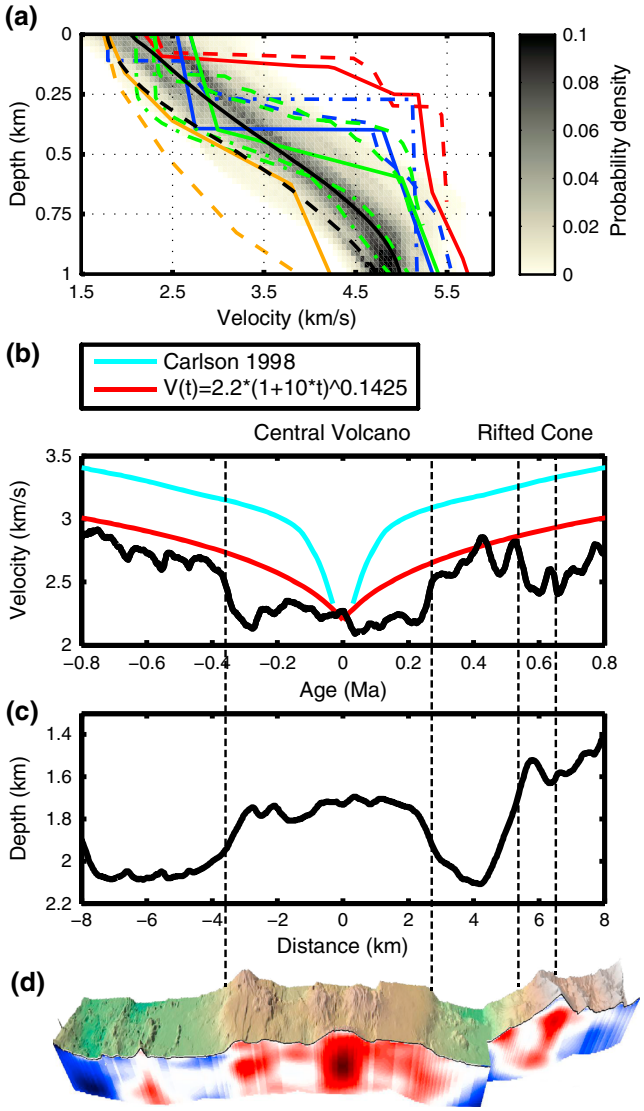

Figure 12. Layer 2A velocities versus age and emplacement history. (a) Velocity distribution at the center of the Lucky Strike segment from Figure 3 compared to different studies at the fast-spreading East Pacific Rise ([*Vera et al.*, 1990] plain red lines and [*Hussenoeder et al.*, 2002b] dashed red lines), at the intermediate spreading Juan de Fuca ridge ([*Cudrak and Clowes*, 1993] plain blue lines, [*McDonald et al.*, 1994] dashed blue lines, and [*Canales et al.*, 2005] dashed dotted blue lines), at the slow spreading Mid-Atlantic Ridge ([*Minshull et al.*, 2003] plain green lines, [*Hussenoeder et al.*, 2002a] dashed green lines, and [*Seher et al.*, 2010c] dashed dotted green lines), and at Lau Basin ([*Jacobs et al.*, 2007] yellow lines). (b) Across-axis average Layer 2A velocity profile computed within the first 200 m bsf. The cyan and blue lines are typical velocity/aging curve presented by *Carlson* [1998, 2004]. The red line is a modification of the *Carlson* [2004] curve to better fit the lower initial velocities at Lucky Strike. (c) Across-axis average depth profile. (d) Three-dimensional velocity anomaly view of the shallow crust beneath the Lucky Strike Volcano.

deformation model [*Gangi and Carlson*, 1996]. In this model, the variation of layer 2A velocity with age, $V(t)$ is written as

$$V(t) = V_0(1 + bt)^m$$

where t is age in Ma, and m and b are constants that depend on the asperity distribution and rate at which grain contacts increase. Our own version of *Carlson* [2004] curve with $V_0 = 2.2$ km/s, $b = 10\,\mathrm{Ma}^{-1}$, and $m = 0.1425$ (which is a better match to the plotted curve in *Carlson* [2004, Figure 1] than the stated values of $V_0 = 2.4$ km/s and $m = 0.14$) is shown in Figure 12b. To obtain the velocity versus age curve for Lucky Strike, we averaged the 3-D velocity model within the first 200 m bsf and in the y direction parallel to the ridge axis (Figures 12b and 12c). The distance across axis was converted to age using a half spreading rate of 1 cm/yr.

©2014. American Geophysical Union. All Rights Reserved.

Comparing the mean velocity profile to bathymetry, reveals that layer 2A velocities are nearly constant at 2.1–2.2 km/s within the central volcano, increase rapidly to reach 2.7 km/s at the transition to axial valley floor, and then follow the trend of the aging curves. The low velocities for the central volcano suggest that it is a young constructional feature relative to the surrounding valley floor (Figure 12) and there has been little increase in the layer 2A velocities since emplacement, an inference consistent with the widespread observation of recent lava deposits.

Average seafloor velocities increase from ~2.2 km/s to ~2.9 km/s over ~0.8 Ma, following the overall trend of our modified version of the aging curve from *Carlson* [2004] (Figure 12b). An earlier compilation of layer 2A measurements [*Carlson*, 1998] suggests an even faster increase in velocity with age, Figure 12b. However, as yet, no measurements along individual flow line profiles have reported a velocity increase this rapid. The smaller increase for young ages, < 2 Ma in the revised curve of *Carlson* [2004] is constrained by the results of *Grevemeyer et al*. [1999] for a transect of ultrafast spread crust formed at 14°S on the East Pacific Rise. A later study by *Nedimovic et al*. [2008] of flow lines from the intermediate spreading Juan de Fuca ridge reports even smaller rates of increase between 0.10 and 0.27 km/s/Ma with the higher rates associated with rapid sedimentation on the east flank of the ridge. *Hussenoeder et al*. [2002a] found means velocities of 2.83 and 2.74 for single MCS profiles on 1.6 and 1.9 Ma crust, respectively. The more rapid velocity increase at Lucky Strike (~0.875 km/s/Myr) indicates that the sealing of small-scale porosity is progressing at normal to enhanced rates, perhaps a reflection of the vigor of the hydrothermal circulation. The mean velocities at the east and west ends of the profile, 2.7 and 2.9 km/s, are comparable.

At the eastern edge of the profile, beyond the boundary fault, average velocities drop down to between ~2.5 and 2.7 km/s, about 0.3–0.4 km/s slower than the aging curve (Figure 12b). This drop may represent a retrograde decrease in seafloor velocity associated with faulting and uplift, inherited background variability in velocity, or changes in the rate of aging. The largest, most deep seated anomaly, is associated with a bathymetric high that *Seher et al*. [2010a] suggest is an old rifted volcanic cone, and it seems likely that, as with the present summital cones, it had lower initial velocity and this has been preserved with age (Figure 12d).

5.3. Volcanism in the Upper Crust

Our analysis shows that the upper oceanic crust at the center of the Lucky Strike segment can be separated in two different distinct units. The first unit, located beneath the median valley, presents a typical layer 2A structure, including velocities ranging between ~2.2 and ~5.2 km/s, a high-velocity gradient at the base of the layer 2A and a bright seismic reflector (2Ab) marking the transition between 2A and 2B (Figures 5, 6, 8, 9, and 10). The structure of the oceanic crust beneath the median valley is thus similar to the one observed at intermediate to fast-spreading ridges with steady state magma chambers except that layer 2A is measurably thicker (~750 m) than is the norm for the axis of fast-spreading segments ($<$250 m). On the other hand, geophysical evidence for a geologically young Lucky Strike Volcano comes from both the tomographic model and seismic reflection profiling.

First, our tomographic structure shows that the average layer 2A velocity within the upper ~200 m across the central volcano is 2.1–2.2 km/s (Figure 12b) in line with expectations for zero-age basaltic oceanic crust. Any lower velocities are in some sense unusual and prompt an explanation. The extremely low-velocity (~1.8–2.2 km/s) and low-reflection amplitude of the summit volcanic mounds could be because they are made solely of pillow lavas with a large amount of void space. In fact, since the eruptions on the central volcano probably tap a single large magma chamber, factors such as the eruption rate and viscosity likely control the nature of the erupted lava and create resolvably heterogeneous structures. Alternatively, the volcanic mounds could have undergone a high degree of fracturing [*Humphris et al*., 2002]. More likely, a combination of these causes is responsible for the low velocity. From the significantly lower velocities in the upper crust *Arnulf et al*. [2011] estimated a maximum porosity range of 25–35% for the summit volcanic mounds, higher than the 10–20% previously suggested by *Seher et al*. [2010a] from OBS data.

Second, multiple subhorizontal seismic reflectors lie within the shallow, high-vertical velocity gradient units of the tomographic model (Figures 8–10) and appear to delimit overlapping volcanic episodes of different ages as presented by *Arnulf et al*. [2012]. These volcanic episodes are most clearly identified within the anomalously low-velocity central volcano. Similarly, the layer 2Aa reflector is nearly ubiquitous beneath the

©2014. American Geophysical Union. All Rights Reserved.

central volcano, and so we suggest that the large lateral continuity of these shallow volcanic layers and of the layer 2Aa surface have a similar origin. These events may represent a quasi-systematic process such as burial of older altered surfaces or paleoseafloors, in other words they may correspond to the boundary between older crust and a newer sequence of eruptions after a hiatus in activity. Thus, the different shallow velocity layers could correspond to different volcanic episodes within the central volcano. This view is in good agreement with the model proposed by *Smith and Cann* [1993], where significant structures within the inner valley floor of the Mid-Atlantic Ridge are an agglomeration of multiple smaller features and eruptions. Therefore, we propose that the crust within the central part of the Lucky Strike segment likely alternates between having a fast spread-like structure of continuous dike injection albeit over a broader injection width and phases of excess magmatism that create the current central volcano or the rifted cones present in the valley walls (Figure 1). If, though, the layer 2Aa reflector is a more general phenomenon, it could correspond to an alteration front that marks the upward progression of hydrothermal mineralization processes through the basaltic crust as described by *Peterson et al*. [1986] albeit with a lower velocity gradient.

In the vicinity of the axial valley faults, the tomography model resolves two elongated zones of anomalously high velocity and an anomalously thin layer 2A. One explanation of this phenomenon is as tectonic thinning of a geological layer of relatively constant thickness, a result of the two axial bounding normal fault systems. This explanation would be independent of whether, as previously suggested, the layer 2A/2B transition is a lithological boundary [*Toomey et al*., 1990; *Harding et al*., 1993], alteration front, or even fracture front [*McClain et al*., 1985; *Burnett et al*., 1989; *Wilcock et al*., 1992; *Christeson et al*., 2007], provided it is relatively unaffected by the fault system.

As previously noted, detailed seafloor geologic mapping of the central volcano summit [*Fouquet et al*., 1994; *Ondréas et al*., 1997, 2009; *Humphris et al*., 2002] has recorded a wide diversity of volcanic deposits. Similarly, seismic heterogeneity within the central volcano is high, notably in the vicinity of the lava lake, surrounding hydrothermal vents, and the summit volcanic edifices (Figures 5 and 6) all located within the neovolcanic region [*Scheirer et al*., 2000]. At these locations, geological mapping and seafloor observations [*Fouquet et al*., 1994; *Ondréas et al*., 1997, 2009; *Scheirer et al*., 2000; *Humphris et al*., 2002] have revealed important variations in the fracture density and differences in the nature of lavas that are strongly correlated with our velocity anomalies, probably through changes in porosity and/or crack distribution and shape. At the three summit edifices and at the northwestern volcanic ridge, the observed low velocities ($<$2.2 km/s) are in good agreement with the presence of highly porous pillow lava deposits. Nevertheless, these velocities are lower than typical layer 2A which also has pillow lavas, so either there is a greater preponderance of pillows versus massive flows or the mounds overall are more porous due perhaps to higher viscosity lavas or enhanced fracturing. In the same way the higher velocities ($>$2.2 km/s, Figures 5 and 6) observed at the lava lake and around the different summital volcanic mounds are well correlated with the lower porosity massive lava flows, polymetallic sulfides, and draped/lobate lavas noted in these regions. We therefore suggest that the narrow vertical zone of slightly higher velocities and probably lower porosities below the lava lake (Figure 6) correspond to an intrusive pipe overlaid by massive lava flows. A low-velocity unit is also observed at the northeastern edge of the central volcano at 550–700 bsf (Figures 5c and 6b). This low-velocity unit is not linked to surface observations but might correspond to a buried paleovolcanic episode that retains part of its initial higher porosity. Similarly, on the eastern wall of the central valley the old rifted volcanic cone appears to have maintained its initial relatively low velocity and high porosity.

6. Conclusions

1. From a combination of "Synthetic Ocean Bottom Experiment" geometry and 3-D traveltime tomography we developed a new methodology that can provide images of the upper oceanic crust with horizontal (~500 m) and vertical (~200 m) resolutions comparable to the length scale of volcanic episodes or local constructive features.
2. The central part of the Lucky Strike segment is shown to be anomalously magmatic compared to the underlying axial valley floor with greater lateral variations in *P* wave velocity structure. Unusually low velocities ($<$2.2 km/s) are observed within the first 100–300 m bsf over the whole central volcano, with the lowest values (~1.8–2.0 km/s) found underneath the three central volcanic cones and the western volcanic ridge.

©2014. American Geophysical Union. All Rights Reserved.

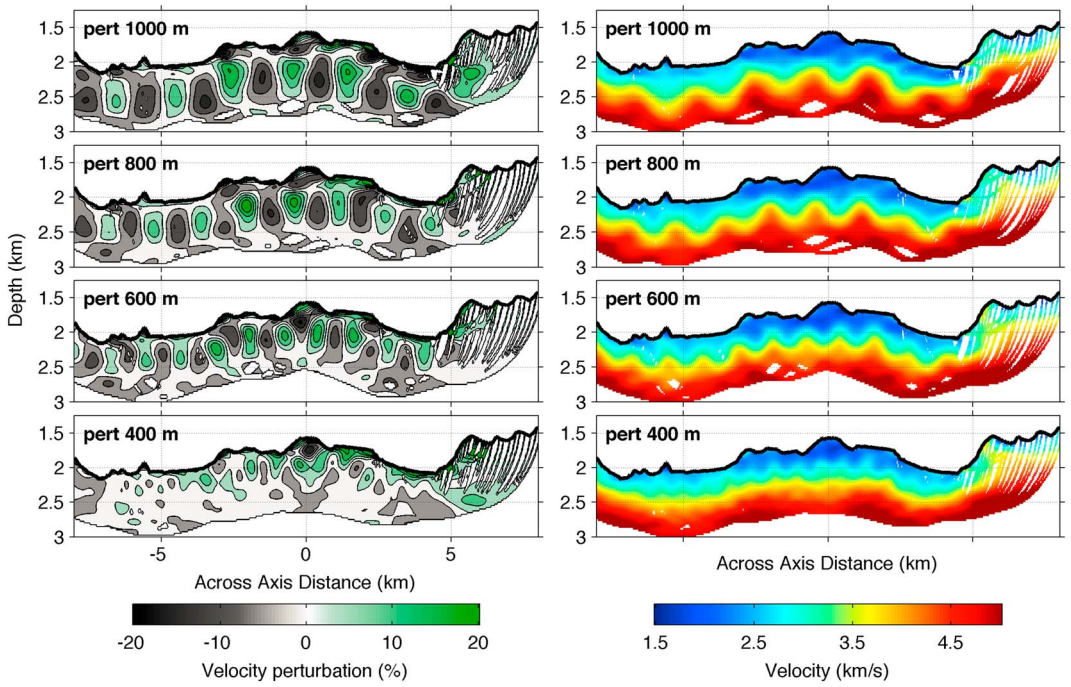

Figure A1. Checkerboard tests for the tomographic inversion. The perturbations added to the best fitting velocity model and used in the forward calculation correspond to 1, 0.8, 0.6, and 0.4 km sinusoidal checkerboards with maximum model perturbation of ± 20% of the background velocities. (a) Perturbations recovered by the inversions. (b) Velocity models recovered by the inversions.

3. The extremely low velocity (~1.8–2.0 km/s) of the summit volcanic mounds are most likely due to a combination of inherent porosity (high-vesicularity pillow basalt) and a high degree of fracturing [*Humphris et al.*, 2002].
4. Within the central volcano, seismic reflection images map several shallow reflectors that may represent a quasi-systematic process such as burial of older altered surfaces or paleoseafloors.
5. We show that layer 2A is thicker (~700–850 m) than is the norm even for slow spreading ridges (375–750 m), which is consistent with the center of the Lucky Strike segment being anomalously magmatic.
6. Finally, we show that hydrothermal sealing of small-scale porosity is progressing at normal to enhanced rates (~0.875 km/s/Myr) over a 0.8 Ma region.

Appendix A: Image Resolution

A1. Checkerboard Tests

Two-dimensional checkerboard tests with different velocity anomaly patterns were conducted to assess the spatial resolution of the final velocity models (Figure A1). Several synthetic velocity models were first created by adding a 2-D sinusoidal velocity perturbation with maximum amplitudes of ±20% of the background velocity to the best fitted model shown in Figure 5a (seismic line 15). The horizontal and vertical wavelengths of the perturbations were chosen to be identical and the half wavelength of the perturbations was set at 1 km, 0.8 km, 0.6 km, and 0.4 km. These synthetic velocity models were then used in the forward calculation to create different sets of synthetic traveltimes using the same geometry as shot during the survey. Next, starting from the best fitting velocity model (Figure 5a, seismic line 15), the synthetic traveltimes were inverted using the same parameters as in our 2-D tomographic inversions. The results of four of these different synthetic tests are shown in Figure A1. For all the tests, a chi-square of 1.0–1.1 and traveltime residuals approaching 10–13 ms were reached. The different resolution tests indicate that features as small as ~ 500 m are well recovered by the inversion from seafloor depth down to approximately 1 km bsf. These results are consistent with the ray density sections from Figure 5d, which show that the uppermost kilometer of crust is densely covered by a multiplicity of turning rays. Furthermore, they can be compared directly to the resolution tests presented by *Seher et al.* [2010a] where only features of 2–4 km wavelengths were resolved by

©2014. American Geophysical Union. All Rights Reserved.

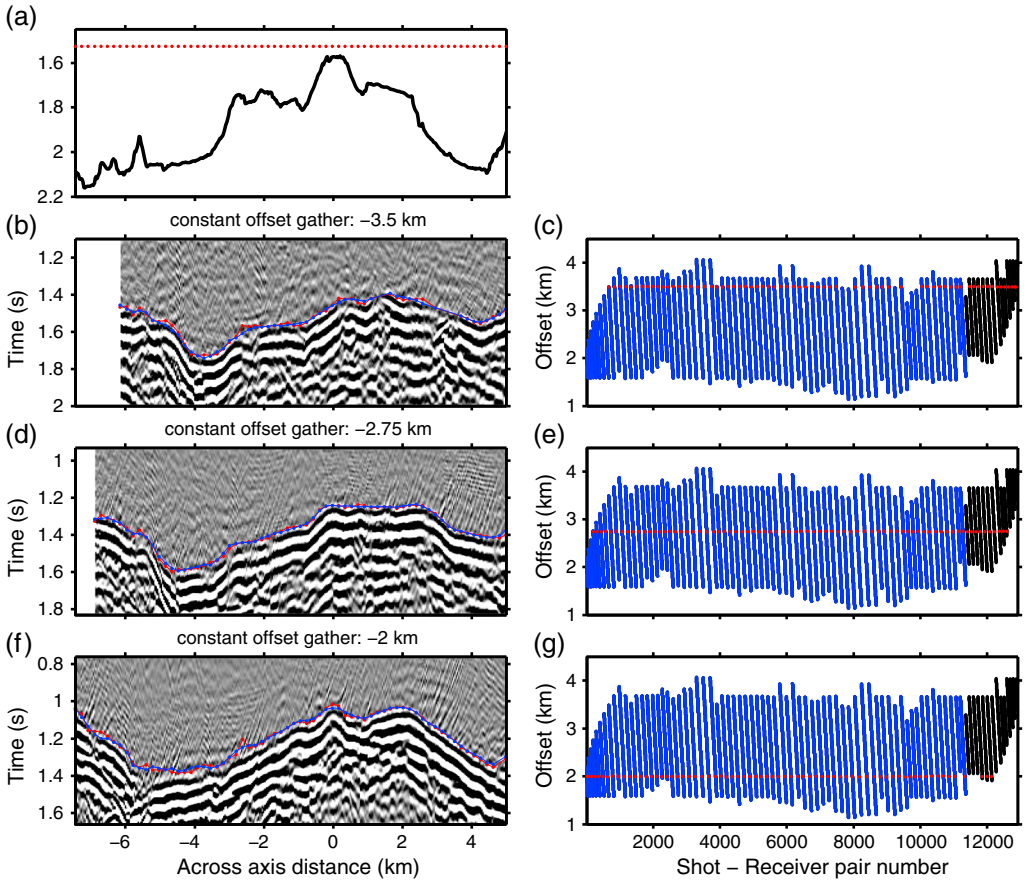

Figure A2. Traveltime picks and model predictions in the Time/Offset domain along seismic line 15. (a) Bathymetry profile along seismic line 15. Red dots mark the location of the inverted shots from the downward extrapolation horizon 1525 m beneath sea surface. Constant offset section at (b) −3.5 km, (d) −2.75 km, and (f) −2 km and (c, e, and g) their corresponding location in the shot-receiver/offset domain. Dotted red and blue lines on Figures A2b, A2d, and A2f correspond, respectively, to our traveltime picks and the final model predictions. Blue and black dots on Figures A2c, A2e, and A2g correspond, respectively, to the shot-receiver pairs at the downward continued horizon 1525 m and 1375 m below sea surface. A total of 12,923 shot-receiver pairs were picked along seismic line 15.

the OBS survey, and to the results of streamer tomography without downward continuation [*Canales et al.*, 2008; *Xu et al.*, 2009], where features of ~1.5 km were meaningfully resolved at subseafloor depths.

These checkerboard tests suggest that the every fifth shot decimation is reasonable. Since we are picking all arrivals in the offset direction a reasonable way of checking the effect of the decimation is to look at the data in constant offset sections (Figure A2). The main variations are captured but both the picks and the model predictions miss a bit at the sharpest corners in the data (Figures A2b, A2d, and A2f). Similarly, we can make an assessment of the likely 3-D resolution without resorting to the large computational expense of a full 3-D test. The distance between the seismic lines in the 3-D data set is ~100 m, approximately one fourth of the smallest half wavelength pattern recovered by our 2-D resolution test. Thus, we would expect that the along-axis horizontal resolution should be similar to the one recovered by our 2-D checkerboard test.

A2. Sensitivity to a High-Velocity Gradient Layer, a "Layer 2A" Test

Vertical and horizontal resolutions are not necessarily identical, and because of the nature of the turning refraction rays one should expect better vertical resolution than horizontal. Figure 5b shows that a 200–350 m thick high-velocity gradient region is imaged within our tomography structure and one might question the vertical resolution of the recovered tomography structure to resolve such a feature. To address this question, a realistic layer 2A velocity model was created by hanging a 1-D velocity model, showing a ~250 m thick high-velocity gradient region with sharp edges, beneath the seafloor (Figures A3a and A3b). This "true" velocity structure was then used in the forward calculation to create a set of synthetic traveltimes. Starting from a simple velocity model presenting a fairly uniform vertical velocity gradient (1–2 s^{-1}, Figures A3c and A3d), the

©2014. American Geophysical Union. All Rights Reserved.

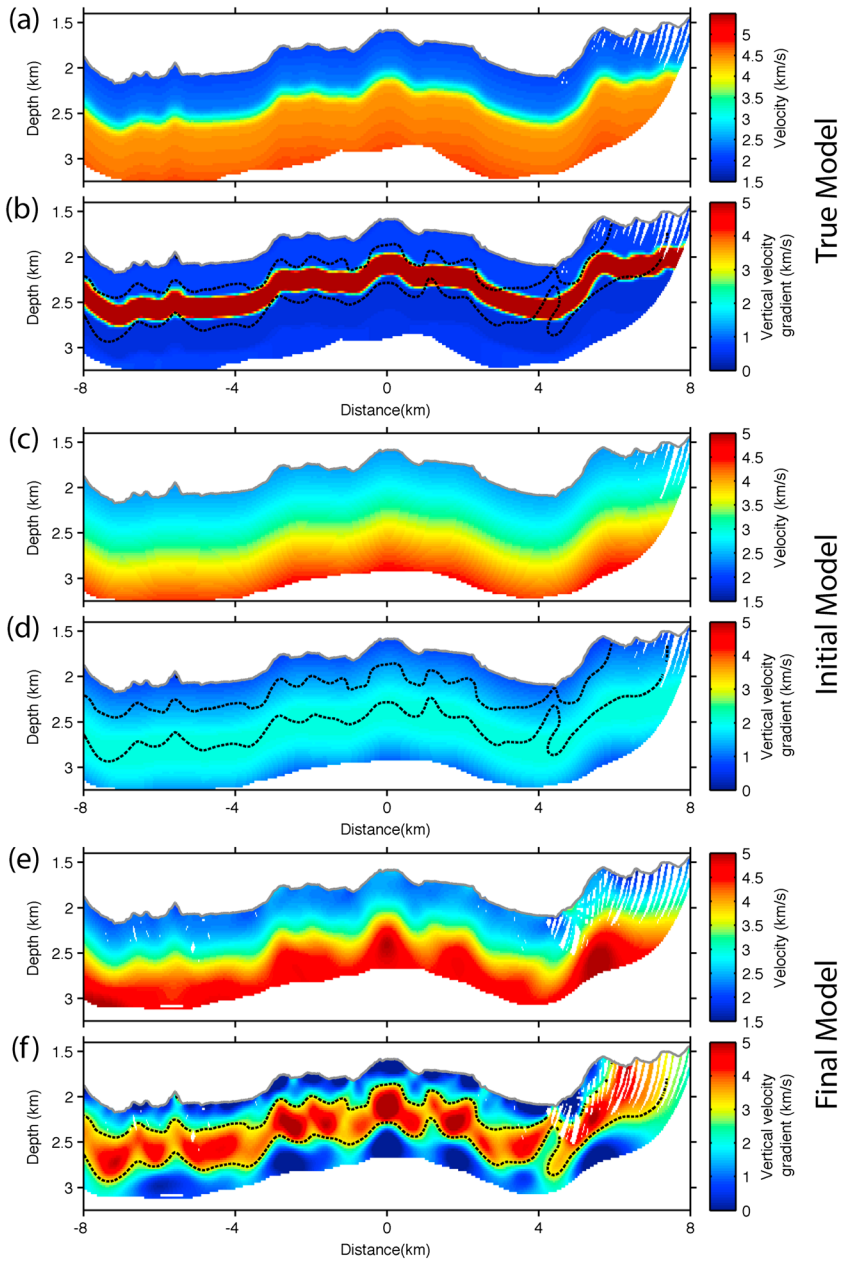

Figure A3. Sensitivity to a high-velocity gradient layer, a layer 2A resolution test. (a) Velocity structure and (b) vertical velocity gradient of the test model. A 1-D velocity model, corresponding to a realistic layer 2A structure was hung underneath the seafloor. (c) Velocity structure and (d) vertical velocity gradient of the inversion starting model. (e) Velocity structure and (f) vertical velocity gradient of the final velocity model. The dashed black lines contour the 3 s^{-1} vertical velocity gradient horizon from the final velocity structure.

synthetic traveltimes were then inverted using the same parameterization as during the survey. The final velocity structure (Figures A3e and A3f) was recovered after nine iterations when a chi-square of 1 and traveltime residuals of ~11 ms were reached. Our final SOBE tomography structure isolates layer 2A as a high-vertical velocity gradient region (Figures A3e, A3f, and A4) and therefore attests to the high-vertical sensitivity of the refraction data. However, the fine-scale gradient structure is not fully resolved by our inversion due to the smoothness regularization operator that is used to stabilize traveltime tomography, which minimizes the gradient and the curvature of the velocity model. In fact, while upper layer 2A and 2B velocities appear to be well resolved, the thickness of the high-velocity gradient region is slightly overestimated and the gradient within this layer is slightly underestimated (Figure A4). Finally, Figure A3 shows how well the velocity gradient contour of ~3 s^{-1} maps the depth and extent of layer 2A within our recovered tomography structure.

©2014. American Geophysical Union. All Rights Reserved.

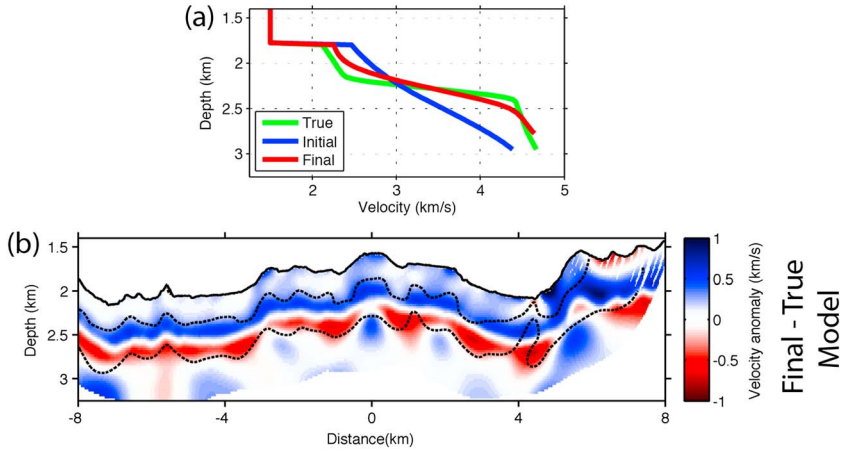

Figure A4. Velocity errors for the layer 2A resolution test. (a) 1-D velocity structure at −1.575 km from the true, initial, and final model from Figure A3. (b) Velocity difference between the final and true velocity structures. The fine-scale gradient structure is not fully resolved by our inversion due to the smoothness regularization operator that is used to stabilize traveltime tomography, which minimizes the gradient and the curvature of the velocity model. The dashed black lines are the 3 s^{-1} vertical velocity gradient contours from the final velocity structure (Figure A1f).

A3. Testing the Low-Velocity Topographic Highs

Figures 5a and 6b show that the central volcano appears to have extremely low velocities in the shallowmost crust and one might be concerned that these are an artifact of the tomographic inversion and the ray coverage with shallow low velocities regions being counterbalanced in the inversion by higher velocities at depth. To address this question, an additional inversion was performed on a model without a shallow, low-velocity layer to see if one was created. This test model was created by smoothing a 1-D velocity model corresponding to the vertical velocity profile located at −5 km across axis for line 14. This 1-D vertical velocity profile was then hung beneath the seafloor, smoothed using a 500 m horizontal and vertical operator, which was used in the forward calculation to create a set of synthetic traveltimes (Figure A5a). The inversion started from the same unsmoothed 1-D velocity model that was used in the initial set of 2-D inversions (Figures A5b), and kept the same parameters as the earlier inversions. The recovered model (Figures A5c) contained no significant low-velocity artifacts within the topographic highs. From this, we conclude that for downward continued data the velocities for the crust from subseafloor depths (~50 m) down to 1 km are reliable and can be interpreted.

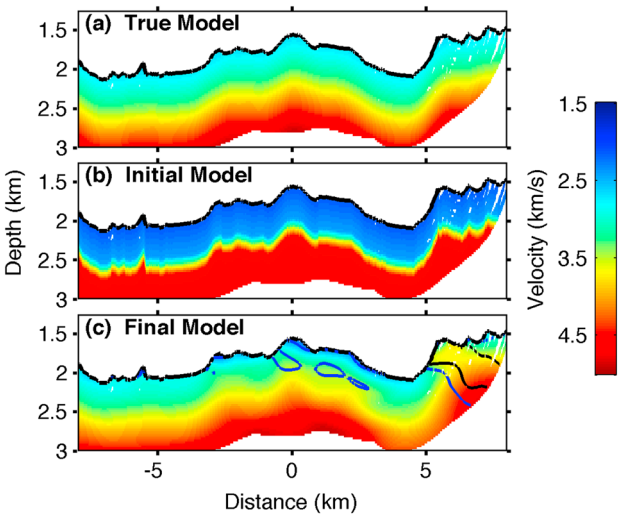

Figure A5. Synthetic inversion performed to test the reliability of the low-velocity topographic highs. (a) Test model. A 1-D velocity model, corresponding to the vertical velocity profile at −5 km across axis on line 14, was hung underneath the seafloor then smoothed using a 500 m laplacian operator. (b) Inversion starting model. (c) Final velocity model. The blue and black contours denote velocity differences of 100 and 200 m/s, respectively, between the test and final model.

©2014. American Geophysical Union. All Rights Reserved.

Acknowledgments
This research was carried out at the Institut de Physique du Globe de Paris as well as at the Scripps Institution of Oceanography. The "Ministère Français de l'enseignement supérieur et de la recherché" supported this work. The National Science Foundation also supported this work by grant OCE-0826481. The Cecil H. and Ida M. Green Foundation for Earth Sciences also supported part of this research. This study also benefited from reviews by Mark Behn, William Wilcock, and an anonymous reviewer. We are grateful to the captain, crew, and seismic team from GENAVIR of cruise SISMOMAR of the RV L'Atalante for their assistance. The INSU MOMAR program funded the acquisition of SISMOMAR project.

References

Arnulf, A. F., S. C. Singh, A. J. Harding, G. M. Kent, and W. Crawford (2011), Strong seismic heterogeneity in Layer 2A near hydrothermal vents at the Mid-Atlantic Ridge, *Geophys. Res. Lett.*, *38*, L13320, doi:10.1029/2011GL047753.

Arnulf, A. F., A. J. Harding, S. C. Singh, G. M. Kent, and W. Crawford (2012), Fine-scale velocity structure of upper oceanic crust from full waveform inversion of downward continued seismic reflection data at the Lucky Strike Volcano, Mid-Atlantic Ridge, *Geophys. Res. Lett.*, *39*, L08303, doi:10.1029/2012GL051064.

Berryhill, J. R. (1979), Wave-equation datuming, *Geophysics*, *44*, 1329–1344.

Berryhill, J. R. (1984), Wave-equation datuming before stack, *Geophysics*, *49*, 2064–2066.

Berryhill, J. R. (1986), Submarine canyons: Velocity replacement by wave-equation datuming before stack, *Geophysics*, *51*, 1572–1579.

Blackman, D. K., and J. A. Collins (2010), Lower crustal variability and the crust/mantle transition at the Atlantis Massif oceanic core complex, *Geophys. Res. Lett.*, *37*, L24303, doi:10.1029/2010GL045165.

Blackman, D. K., et al. (2002), Geology of the Atlantis Massif (Mid-Atlantic Ridge, 30°N): Implications for the evolution of an ultramafic oceanic core complex, *Mar. Geophys. Res.*, *23*, 443–469, doi:10.1023/B:MARI.0000018232.14085.75.

Boschi, C., G. L. Früh-Green, A. Delacour, J. A. Karson, and D. S. Kelley (2006), Mass transfer and fluid flow during detachment faulting and development of an oceanic core complex, Atlantis Massif (MAR 30°N), *Geochem. Geophys. Geosyst.*, *7*, Q01004, doi:10.1029/2005GC001074.

Burnett, M. S., D. W. Caress, and J. A. Orcutt (1989), Tomographic image of the magma chamber at 12°50′N on the East Pacific Rise, *Nature*, *339*, 206–208.

Canales, J. P., R. S. Detrick, S. M. Carbotte, G. M. Kent, J. B. Diebold, A. J. Harding, J. Babcock, M. R. Nedimovic, and E. Van Ark (2005), Upper crustal structure and axial topography at intermediate spreading ridges: Seismic constraints from the southern Juan de Fuca Ridge, *J. Geophys. Res.*, *110*, B12104, doi:10.1029/2005JB003630.

Canales, J. P., B. E. Tucholke, M. Xu, J. A. Collins, and D. L. DuBois (2008), Seismic evidence for large-scale compositional heterogeneity of the oceanic core complexes, *Geochem. Geophys. Geosyst.*, *9*, Q08002, doi:10.1029/2008GC002009.

Cann, J. R., D. K. Blackman, D. K. Smith, E. McAllister, B. Janssen, S. Mello, E. Avgerinos, A. R. Pascoe, and J. Escartín (1997), Corrugated slip surfaces formed at ridge–transform intersections on the Mid-Atlantic Ridge, *Nature*, *385*, 329–332, doi:10.1038/385329a0.

Cannat, M., et al. (1995), Thin crust, ultramafic exposures, and rugged faulting patterns at the Mid-Atlantic Ridge (22°–24°N), *Geology*, *23*(1), 49–52, doi:10.1130/00917613(1995)023<0049:TCUEAR>2.3.CO;2.

Cannat, M., et al. (1999), Mid-Atlantic Ridge—Azores hotspot interactions: Along-axis migration of a hotspot-derived event of enhanced magmatism 10 to 4 Ma ago, *Earth Planet. Sci. Lett.*, *173*, 257–269, doi:10.1016/S0012-821X(99)00234-4.

Carbotte, S. M., and K. Macdonald (1992), East Pacific Rise 8°–10°30′N: Evolution of ridge segments and discontinuities from SeaMARC II and three-dimensional magnetic studies, *J. Geophys. Res.*, *97*(B5), 6959–6982.

Carbotte, S. M., A. Solomon, and G. Ponce-Correa (2000), Evaluation of morphological indicators of magma supply and segmentation from a seismic reflection study of the East Pacific Rise 15°30′–17°N, *J. Geophys. Res.*, *105*(B2), 2737–2759.

Carlson, R. (1998), Seismic velocities in the uppermost oceanic crust: Age dependence and the fate of layer 2A, *J. Geophys. Res.*, *103*(B4), 7069–7077, doi:10.1029/97JB03577.

Carlson, R. L. (2004), Seismic properties of Layer 2A at 11 Ma: Results of a vertical seismic profile at Ocean Drilling Program Site 1243, *Geophys. Res. Lett.*, *31*, L17601, doi:10.1029/2004GL020598.

Christeson, G., G. Purdy, and G. Fryer (1994), Seismic constraints on shallow crustal emplacement processes at the fast spreading East Pacific Rise, *J. Geophys. Res.*, *99*, 17,957–17,973.

Christeson, G., G. M. Kent, G. M. Purdy, and R. S. Detrick (1996), Extrusive thickness variability at the East Pacific Rise, 9°–10°N: Constraints from seismic techniques, *J. Geophys. Res.*, *101*(B2), 2859–2873.

Christeson, G. L., K. D. McIntosh, and J. A. Karson (2007), Inconsistent correlation of seismic layer 2a and lava layer thickness in oceanic crust, *Nature*, *445*, 418–421.

Collins, J. A., D. K. Blackman, A. Harris, and R. L. Carlson (2009), Seismic and drilling constraints on velocity structure and reflectivity near IODP Hole U1309D on the central dome of Atlantis Massif, Mid-Atlantic Ridge 30°N, *Geochem. Geophys. Geosyst.*, *10*, Q01010, doi:10.1029/2008GC002121.

Combier, V. (2007), Mid-ocean ridge processes. Insights from 3D reflection seismics at 9°N OSC on the East Pacific Rise, and the Lucky Strike Volcano on the Mid-Atlantic Ridges, PhD thesis, Laboratoire de Geosciences Marines, Institut de Physique du Globe de Paris, Paris, France.

Combier, V., S. C. Singh, M. Cannat, and J. Escartín (2008), Mechanical decoupling and thermal structure at the East Pacific Rise axis 9°N: Constraints from axial magma chamber geometry and seafloor structures, *Earth Planet. Sci. Lett.*, *272*, 19–28, doi:10.1016/j.epsl.2008.03.046.

Cudrak, C. F., and R. M. Clowes (1993), Crustal structure of Endeavour Ridge segment, Juan de Fuca Ridge, From a detailed seismic refraction survey, *J. Geophys. Res.*, *98*(B4), 6329–6349.

Demets, C., R. G. Gordon, D. F. Argus, and S. Stein (1994), Effect of recent revisions to the geomagnetic reversal time scale on estimates of current plate motions, *Geophys. Res. Lett.*, *21*, 2191–2194.

Detrick, R. S., P. Buhl, E. Vera, J. Mutter, J. Orcutt, J. Madsen, and T. Brocher (1987), Multichannel seismic imaging of a crustal magma chamber along the East Pacific Rise between 9°N and 13°N, *Nature*, *326*, 35–41.

Detrick, R., J. Mutter, P. Buhl, and I. Kim (1990), No evidence from multichannel reflection data for a crustal magma chamber in the MARK area on the Mid-Atlantic Ridge, *Nature*, *347*, 61–64, doi:10.1038/347061a0.

Detrick, R. S., H. D. Needham, and V. Renard (1995), Gravity anomalies and crustal thickness variations along the Mid-Atlantic Ridge between 33°N and 40°N, *J. Geophys. Res.*, *100*, 3767–3787.

Dick, H. J. B., M. A. Tivey, and B. E. Tucholke (2008), Plutonic foundation of a slow-spreading ridge segment: The oceanic core complex at Kane Megamullion, 23°30′N, 45°20′W, *Geochem. Geophys. Geosyst.*, *9*, Q05014, doi:10.1029/2007GC001645.

Dziak, R., D. Smith, D. Bohnenstiehl, C. Fox, D. Desbruyeres, H. Matsumoto, M. Tolsoty, and D. Fornari (2004), Evidence of a recent magma dike intrusion at the slow spreading Lucky Strike segment, Mid-Atlantic Ridge, *J. Geophys. Res.*, *109*, B12102, doi:10.1029/2004JB003141.

Escartín, J., M. Cannat, G. Pouliquen, and A. Rabain (2001), Crustal thickness of V-shaped ridges south of the Azores: Interaction of the Mid-Atlantic Ridge (36°N–39°N) and the Azores hot spot, *J. Geophys. Res.*, *106*(B10), 21,719–21,735, doi:10.1029/2001JB000224.

Fouquet, Y., J.-L. Charlou, I. Costa, J.-P. Donval, J. Radford-Knoery, H. Pellé, H. Ondréas, N. Lourenço, M. Ségonzac, and M. Kingston Tivey (1994), A detailed study of the Lucky Strike hydrothermal site and discovery of a new hydrothermal site: Menez Gwen: Preliminary results of the DIVA1 cruise (5–29 May, 1994), *InterRidge News*, *3*(2), 14–17.

Fouquet, Y., H. Ondréas, J.-L. Charlou, J.-P. Donval, J. Radford-Knoery, I. Costa, N. Lourenço, and M. Tivey (1995), Atlantic lava lakes and hot vents, *Nature*, *377*, 201, doi:10.1038/377201a0.

Gangi, A. F., and R. L. Carlson (1996), An asperity-deformation model for effective pressure, *Tectonophysics*, *256*, 241–251.

©2014. American Geophysical Union. All Rights Reserved.

Gazdag, J. (1978), Wave equation migration with the phase-shift method, *Geophysics*, *43*, 1342–1351.
Grevemeyer, I., N. Kaul, H. Villinger, and W. Weigel (1999), Hydrothermal activity and the evolution of the seismic properties of upper oceanic crust, *J. Geophys. Res.*, *104*(B3), 5069–5079.
Harding, A., J. Orcutt, M. Kappus, E. Vera, J. Mutter, R. Buhl, R. Detrick, and T. Brocher (1989), Structure of young oceanic crust at 13°N on the East Pacific Rise from expanding spread profile, *J. Geophys. Res.*, *94*(B9), 12,163–12,196, doi:10.1029/JB094iB09p12163.
Harding, A. J., G. M. Kent, and J. A. Orcutt (1993), A multichannel seismic investigation of the upper crustal structure at 9°N on the East Pacific Rise: Implications for crustal accretion, *J. Geophys. Res.*, *98*, 13,925–13,944.
Harding, A. J., G. M. Kent, D. K. Blackman, S. C. Singh, and J.-P. Cannales (2007), A new method for MCS refraction data analysis of the uppermost section at a Mid-Atlantic Ridge core complex, *Eos Trans. AGU*, 88(52), Fall Meet. Suppl., Abstract S12A-03.
Henig, A. S., D. K. Blackman, A. J. Harding, J.-P. Canales, and G. M. Kent (2012), Downward continued multichannel seismic refraction analysis of Atlantis Massif oceanic core complex, 30°N, Mid-Atlantic Ridge, *Geochem. Geophys. Geosyst.*, *13*, Q0AG07, doi:10.1029/2012GC004059.
Hooft, E. E. E., R. S. Detrick, D. R. Toomey, J. A. Collins, and J. Lin (2000), Crustal thickness and structure along three constraining spreading segments of the Mid-Atlantic Ridge, 33.5°–35°N, *J. Geophys. Res.*, *105*(B4), 8205–8226.
Humphris, S. E., D. J. Fornari, D. S. Scheirer, C. R. German, and L. M. Parson (2002), Geotectonic setting of hydrothermal activity on the summit of Lucky Strike Seamount (37°17′N, Mid-Atlantic Ridge), *Geochem. Geophys. Geosyst.*, *3*(8), 1049, doi:10.1029/2001GC000284.
Hussenoeder, S. A., G. M. Kent, and R. S. Detrick (2002a), Upper crustal seismic structure of the slow spreading Mid-Atlantic Ridge, 35°N: Constraints on volcanic emplacement processes, *J. Geophys. Res.*, *107*(B8), 2156, doi:10.1029/2001JB001691.
Hussenoeder, S. A., R. S. Detrick, G. M. Kent, H. Schouten and A. J. Harding (2002b), Fine-scale seismic structure of young upper crust at 17°20′ S on the fast spreading East Pacific Rise, *J. Geophys. Res.*, *107*(B8), 2158, doi:10.1029/2001JB001688.
Jacobs, A. M., A. J. Harding, and G. M. Kent (2007), Axial crustal structure of the Lau back-arc basin from velocity modeling of multichannel seismic data, *Earth Planet. Sci. Lett.*, *259*, 239–255.
Kent, G. M., A. J. Harding, and J. A. Orcutt (1993), Distribution of magma beneath the East Pacific Rise between the Clipperton transform and the 9°17′N deval from forward modeling of common depth point data, *J. Geophys. Res.*, *98*, 13,945–13,969.
Kent, G. M., et al. (2000), Evidence from three-dimensional seismic reflectivity images for enhanced melt supply beneath mid-ocean-ridge discontinuities, *Nature*, *406*, 614–618.
Langmuir, C., et al. (1997), Hydrothermal vents near a mantle hot spot: The Lucky Strike vent field at 37°N on the Mid-Atlantic Ridge, *Earth Planet. Sci. Lett.*, *148*, 69–91.
Macdonald, K. (1982), Mid-ocean ridges: Fine scale tectonic, volcanic and hydrothermal processes within the plate boundary zone, *Ann. Rev. Earth Planet. Sci.*, *10*, 155–90.
Macdonald, K. (2001), Mid-ocean ridge tectonics, volcanism and geomorphology, in *Encyclopedia of Ocean Sciences*, pp. 1798–1813, Academic, London, U.K.
Macdonald, K. C., and P. J. Fox (1983), Overlapping spreading centres: New accretion geometry on the East Pacific Rise, *Nature*, *301*, 55–58.
McClain, J. S., J. A. Orcutt, and M. Burnett (1985), The East Pacific Rise in cross section: A seismic model, *J. Geophys. Res.*, *90*, 8627–8640.
McDonald, M. A., S. C. Webb, J. A. Hildebrand, and B. D. Cornuelle (1994), Seismic structure and anisotropy of the Juan de Fuca Ridge at 45°N, *J. Geophys. Res.*, *99*(B3), 4857–4873.
Minshull, T. A., N. J. Bruguier, and J. M. Brozena (2003), Seismic structure of the Mid-Atlantic Ridge, 8–9°S, *J. Geophys. Res.*, *108*(B11), 2513, doi:10.1029/2002JB002360.
Miranda, J., J. Luis, N. Lourenço, and F. Santos (2005), Identification of the magnetization low of the Lucky Strike hydrothermal vent using surface magnetic data, *J. Geophys. Res.*, *110*, B04103, doi:10.1029/2004JB003085.
Moreira, M., and C. J. Allegre (2002), Rare gas systematics on Mid-Atlantic Ridge (37–40°N), *Earth Planet. Sci. Lett.*, *198*, 401–416, doi:10.1016/S0012-821X(02)00519-8.
Moser, T. J. (1991), Shortest path calculation of seismic rays, *Geophysics*, *56*, 59–67.
Nedimovic, M. R., S. M. Carbotte, J. B. Diebold, A. J. Harding, J. P. Canales, and G. M. Kent (2008), Upper crustal evolution across the Juan de Fuca ridge flanks, *Geochem. Geophys. Geosyst.*, *9*, Q09006, doi:10.1029/2008GC002085.
Newman, K. R., M. R. Nedimovic, J. P. Canales, and S. M. Carbotte (2011), Evolution of seismic layer 2B across the Juan de Fuca Ridge from hydrophone streamer 2-D traveltime tomography, *Geochem. Geophys. Geosyst.*, *12*, Q05009, doi:10.1029/2010GC003462.
Ondréas, H., Y. Fouquet, M. Voisset, and J. Radford-Knoery (1997), Detailed study of three contiguous segments of the Mid-Atlantic Ridge, south of the Azores (37°N to 38°30′N), using acoustic imaging coupled with submersible observations, *Mar. Geophys. Res.*, *19*, 231–255.
Ondréas, H., M. Cannat, Y. Fouquet, A. Normand, P.-M. Sarradin, and J. Sarrazin (2009), Recent volcanic events and the distribution of hydrothermal venting at the Lucky Strike hydrothermal field, Mid-Atlantic Ridge, *Geochem. Geophys. Geosyst.*, *10*, Q02006, doi:10.1029/2008GC002171.
Orcutt, J. A., B. L. N. Kennett, and L. M. Dorman (1976), Structure of the East Pacific Rise from an ocean bottom seismometer array, *Geophys. J. R. Astron. Soc.*, *45*, 305–20.
Peterson, C., R. Duncan, and K. F. Scheidegger (1986), Sequence and longevity of basalt alteration at Deep Sea Drilling Project Site 597, *Initial Rep. Deep Sea Drill. Proj.*, *92*, 505–515.
Scheirer, D. S., D. J. Fornari, S. E. Humphris, and S. Lerner (2000), High-resolution mapping using the DSL-120 sonar system: Quantitative assessment of sidescan and phase-bathymetry data from the Lucky Strike segment of the mid-Atlantic Ridge, *Mar. Geophys. Res.*, *21*, 121–142.
Seher, T., S. C. Singh, W. Crawford, and J. Escartin (2010a), Upper crustal velocity structure beneath the central Lucky Strike Segment from seismic refraction measurements, *Geochem. Geophys. Geosyst.*, *11*, Q05001, doi:10.1029/2009GC002894.
Seher, T., W. C. Crawford, S. C. Singh, M. Cannat, V. Combier, and D. Dusunur (2010b), Crustal velocity structure of the Lucky Strike segment of the Mid-Atlantic Ridge (37°N) from seismic refraction measurements, *J. Geophys. Res.*, *115*, B03103, doi:10.1029/2009JB006650.
Seher, T., W. C. Crawford, S. C. Singh, and M. Cannat (2010c), Seismic layer 2A variations in the Lucky Strike segment at the Mid-Atlantic Ridge from reflection measurements, *J. Geophys. Res.*, *115*, B07107, doi:10.1029/2009JB006783.
Sigloch, K., and G. Nolet (2006), Measuring finite-frequency body-wave amplitudes and traveltimes, *Geophys. J. Int.*, *167*, 271–287.
Singh, S. C., G. M. Kent, J. S. Collier, A. J. Harding, and J. A. Orcutt (1998), Melt to mush variations in crustal magma properties along the ridge crest at the southern East Pacific Rise, *Nature*, *394*, 874–878.
Singh, S. C., W. C. Crawford, H. Carton, T. Seher, V. Combier, M. Cannat, J. Pablo Canales, D. Düsünür, J. Escartin, and J. M. Miranda (2006), Discovery of a magma chamber and faults beneath a Mid-Atlantic Ridge hydrothermal field, *Nature*, *442*, 1029–1032.
Sinha, M. C., S. C. Constable, C. Peirce, A. White, G. Heinson, L. M. Mac Gregor, and D. A. Navin (1998), Magmatic processes at slow spreading ridges: Implications of the RAMESSES experiment at 57°45′N on the Mid-Atlantic Ridge, *Geophys. J. Int.*, *135*, 731–745.
Smith, D., and J. Cann (1993), Building the crust at the Mid-Atlantic Ridge, *Nature*, *365*, 707–715, doi:10.1038/365707a0.

©2014. American Geophysical Union. All Rights Reserved.

Thibaud, R., P. Gente, and M. Maia (1998), A systematic analysis of the Mid-Atlantic Ridge morphology and gravity between 15°N and 40°N: Constraints of the thermal structure, *J. Geophys. Res.*, *103*(B10), 24,223–24,243.

Tolstoy, M., A. Harding, and J. Orcutt (1993), Crustal thickness on the Mid-Atlantic Ridge: Bull's-eye gravity anomalies and focused accretion, *Science*, *262*(5134), 726–729, doi:10.1126/science.262.5134.726.

Toomey, D. R., G. M. Purdy, S. C. Solomon, and W. S. D. Wilcock (1990), The three-dimensional seismic velocity structure of the East Pacific Rise near latitude 9°30'N, *Nature*, *347*, 639–645.

Tucholke, B. E., and J. Lin (1994), A geological model for the structure of ridge segments in slow spreading ocean crust, *J. Geophys. Res.*, *99*, 11,937–11,958, doi:10.1029/94JB00338.

Van Avendonk, H. J. A., D. J. Shillington, W. S. Holbrook, and M. J. Hornbach (2004), Inferring crustal structure in the Aleutian island arc from a sparse wide-angle seismic data set, *Geochem. Geophys. Geosyst.*, *5*, Q08008, doi:10.1029/2003GC000664.

Vera, E. E., and J. B. Diebold (1994), Seismic imaging of oceanic layer 2A between 9°30'N and 10°N on the East Pacific Rise from two-ship wide-aperture profiles, *J. Geophys. Res.*, *99*(B2), 3031–3041.

Vera, E. E., J. C. Mutter, P. Buhl, J. A. Orcutt, A. J. Harding, M. E. Kappus, R. S. Detrick, and T. M. Brocher (1990), The structure of 0- to 0.2-m.y.-Old Oceanic Crust at 9°N on the East Pacific Rise from expanded spread profiles, *J. Geophys. Res.*, *95*(B10), 15,529–15,556.

White, R., D. McKenzie, and R. O'Nions (1992), Oceanic crustal thickness from seismic measurements and rare earth element inversions, *J. Geophys. Res.*, *97*(B13), 19,683–19,715, doi:10.1029/92JB01749.

Wilcock, W. S. D., S. C. Solomon, G. M. Purdy, and D. R. Toomey (1992), The seismic attenuation structure of a fast-spreading mid-ocean ridge, *Science*, *258*, 1470–1474.

Xu, M., J.-P. Canales, B. E. Tucholke, and D. L. Dubois (2009), Heterogeneous seismic velocity structure of the upper litosphere at Kane oceanic core complex, Mid-Atlantic Ridge, *Geochem. Geophys. Geosyst.*, *10*, Q10001, doi:10.1029/2009GC002586.

Zelt, B. C., B. Taylor, J. R. Weiss, A. M. Goodliffe, M. H. Sachpazi, and A. Hirn (2004), Streamer tomography velocity models for the Gulf of Corinth and Gulf of Itea, Greece, *Geophys. J. Int.*, *159*, 333–346.

©2014. American Geophysical Union. All Rights Reserved.